DC-BL: Flexible Delay-Doppler Domain Channel Estimation via Decoupled Bayesian Learning

Xinbo Gao, *Graduate Student Member, IEEE*, Chenyuan Feng, *Member, IEEE*, Minjie Tang, *Member, IEEE*,
Zunqi Li, *Graduate Student Member, IEEE*, Xiaojie Fang, *Member, IEEE*, Zhuoming Li,
and Tony Q. S. Quek, *Fellow, IEEE*

***Abstract*—Orthogonal Time Frequency Space (OTFS) modulation has shown remarkable robustness in high-mobility scenarios by effectively mitigating the detrimental effects of Doppler shifts. However, accurate channel estimation for OTFS systems remains a challenging problem due to issues such as energy dispersion caused by fractional Doppler shifts, limited exploitation of inherent delay-Doppler domain sparsity, and prohibitive computational complexity. In this work, we propose a novel decoupled channel estimation framework that decomposes the delay-Doppler (DD) domain channel into separate delay and Doppler components. This decoupling facilitates a more efficient and targeted utilization of channel structures in each domain. Building upon this framework, we develop a novel estimation algorithm based on decoupled Bayesian learning (DC-BL), which leverages virtual grids and integration-based sensing matrices to achieve super-resolution channel recovery. Notably, the proposed method retains adaptability even under low-resolution grid settings. To address such scenarios, we further design a specialized Bayesian estimation algorithm optimized for coarse-granularity grids. Both algorithms incorporate a sparsity-aware mechanism to eliminate redundant channel taps, thereby significantly reducing model dimensionality and computational burden. Extensive simulation results demonstrate that the proposed methods consistently outperform existing state-of-the-art approaches in terms of estimation accuracy and efficiency.**

***Index Terms*—Orthogonal time frequency space (OTFS), decoupled channel estimation, Bayesian learning, low computational complexity.**

I. INTRODUCTION

IN future wireless systems, it is a critical requirement to ensure reliable data transmission [1] in vehicular-to-everything (V2X) applications such as autonomous driving, collision avoidance, and navigation [2]–[5]. These V2X application scenarios are characterized by rapidly time-varying channels with substantial Doppler spreads, posing significant challenges for maintaining link reliability and system performance. Orthogonal frequency division multiplexing (OFDM), widely adopted in 4G and 5G systems, performs well in quasi-static frequency-selective channels. However, its susceptibility to inter-carrier interference (ICI) severely degrades performance in fast time-varying environments [6]–[8]. This limitation has driven interest in alternative modulation schemes that are more resilient to Doppler-induced impairments.

Recently, orthogonal time frequency space (OTFS) modulation has emerged as a promising solution for high-mobility wireless communication, offering intrinsic advantages over OFDM [9], [10]. Unlike traditional one-dimensional (1D) modulation techniques, OTFS employs a two-dimensional (2D) signal representation by mapping information symbols onto the delay-Doppler (DD) domain using pre-defined localized pulses [9], [10]. The DD-domain representation is transformed into the time-frequency domain via symplectic Fourier transforms, enabling each symbol to be distributed across the entire time-frequency grid within a transmission frame. This structure allows OTFS to harness full time-frequency diversity and to combat channel fading more effectively than OFDM [11]. Moreover, the quasi-stationary nature of the DD-domain channel not only provides statistical stability but also enables a compact representation of the channel parameters and their sparsity.

A. Related Work

Accurate channel estimation is vital for ensuring robust data transmission in OTFS systems, especially in dynamic wireless environments. Numerous methods have been proposed to tackle the associated challenges. In [12], a pilot embedding scheme was introduced that integrates pilot, guard, and data symbols within a single OTFS frame. A threshold-based estimation algorithm was further developed to extract channel information. The concept was extended to MIMO-OTFS systems in [13], where orthogonality between pilot symbols for different antennas was maintained via guard intervals. In [14], a DNN-based OTFS channel estimation framework was proposed. With a simple network architecture, it effectively estimates channel parameters and achieves comparable performance to threshold-based methods with much lower pilot power. This work introduces a new perspective for addressing the OTFS channel estimation problem. However, while these guard-based designs help avoid pilot-data interference, they inevitably compromise spectral efficiency. To address this

---

Manuscript created 14 June 2025. *(Corresponding author: Zhuoming Li; Minjie Tang)*

Xinbo Gao, Zunqi Li and Xiaojie Fang are with the School of Electronics and Information Engineering, Harbin Institute of Technology, Harbin 150001, China, and also with the Science and Technology on Communication Networks Laboratory, Shijiazhuang 050080, China (e-mail: gaoxinbo0329@hit.edu.cn; lizunqi@stu.hit.edu.cn; fangxiaojie@hit.edu.cn).

Zhuoming Li are with the School of Electronics and Information Engineering, Harbin Institute of Technology, Harbin 150001, China (e-mail: zhuoming@hit.edu.cn).

Minjie Tang is with the Department of Communication Systems, EURECOM, France (e-mail: Minjie.Tang@eurecom.fr).

Chenyuan Feng is with the Department of Computer Science, University of Exeter, Exeter EX4 4QJ, U.K. (email: c.feng@exeter.ac.uk).

Tony Q. S. Quek is with the Information Systems Technology and Design Pillar, Singapore University of Technology and Design, Singapore (e-mail: tonyquek@sutd.edu.sg)

issue, superimposed pilot-based estimation schemes have been explored, offering improved spectral utilization by overlapping pilot and data symbols [15], [16].

Traditional training-based channel estimation techniques are often suboptimal in OTFS systems due to the inherent sparsity of delay-Doppler (DD) domain channels—particularly in multipath-rich scenarios [17]. As a result, compressed sensing (CS) approaches have gained traction. For instance, [18] introduced a 3D-structured orthogonal matching pursuit (3D-SOMP) algorithm that exploits sparsity across delay-Doppler-angle (DDA) domain for downlink channel estimation in massive MIMO-OTFS systems. However, this method assumes integer Doppler shifts and struggles with performance degradation when fractional Doppler effects are present. To address this, [19] proposed a modified sensing matrix that enhances estimation accuracy and reduces memory requirements in fractional Doppler environments. Similarly, [20] employed Newtonized orthogonal matching pursuit (NOMP) for channel parameter recovery in MIMO-OTFS systems. Nevertheless, these greedy algorithms generally fall short in terms of estimation accuracy and robustness.

An alternative and increasingly popular line of research involves sparse Bayesian learning (SBL) [21]. In [22], an SBL-based framework was integrated into OTFS system to estimate the channel state information (CSI), demonstrating superior performance over orthogonal matching pursuit (OMP). Further advancements include the row-group Bayesian learning (RG-BL) method developed in [23], which leverages structural sparsity across antenna elements. Despite these advancements, most prior works are constrained by the assumption of integer Doppler shifts, which limits their practical deployment. To address this, off-grid SBL techniques were introduced in [24], where the DD domain was discretized into finer virtual grids. Off-grid parameters were modeled as hyperparameters in the SBL framework, enabling the estimation of fractional delays and Doppler shifts. While 1D off-grid SBL improves normalized mean square error (NMSE) over on-grid methods, it suffers from high computational complexity. The 2D variant, although more efficient, exhibits performance degradation and lacks compatibility with practical OTFS waveforms. A hybrid 1&2D fractional model was later proposed in [25] to balance accuracy and complexity. Based on this model, a 2D off-grid decomposition and combination scheme is devised to effectively balance the accuracy and computational workload. However, there are some limitations on the 2D off-grid decomposition and combination scheme. Firstly, the scheme designed based on the ideal waveform cannot be applied to OTFS systems with a rectangular waveform. Besides, the scheme imposes strict requirements on the arrangement of the pilots.

B. Motivations & Contributions

Although substantial progress has been made in OTFS channel estimation, existing approaches still encounter several limitations, including sensitivity to fractional delays and Doppler shifts, high computational complexity, insufficient exploitation of domain-specific channel structures, and limited waveform compatibility. These limitations underscore the need for a more flexible and efficient channel estimation paradigm. To address these issues, we propose an efficient decoupled channel estimation framework that separates the DD-domain channel into independent delay and Doppler components. Unlike prior studies such as [24], [25], which primarily focus on bi-orthogonal waveforms, our framework supports both ideal and practical pulse shapes, including rectangular waveforms commonly used in real-world systems. While high-resolution virtual grids can significantly improve estimation accuracy, they also introduce heavy computational burdens. To balance this trade-off, we develop a flexible algorithmic strategy that maintains high performance even under low-resolution grid settings. A parametric dictionary learning model is employed to enhance estimation robustness in such scenarios. The main contributions are summarized as follows:

- **Novel Decoupled Channel Estimation Framework**: We propose a novel framework that decomposes the DD-domain channel into separate delay and Doppler domain components through integration-based sensing matrices. This structure enables domain-specific algorithm design and is applicable to both bi-orthogonal and rectangular pulse shaping filters.
- **Decoupled Bayesian Learning (DC-BL) Algorithm**: Building on the framework, we design a decoupled Bayesian learning (DC-BL) algorithm that independently estimates the delay and Doppler domain components. High-resolution virtual grids are introduced to achieve super-resolution estimation performance.
- **Low-Resolution Adaptation via Dictionary Learning**: For practical scenarios with coarse virtual grids, we further develop an alternative DC-BL algorithm. By incorporating a parametric dictionary learning strategy, the alternative algorithm effectively compensates for resolution limitations and enhances estimation accuracy.
- **Model Dimensionality Reduction and Efficiency**: The proposed algorithms exploit the inherent sparsity of the channel by discarding non-essential components, thereby reducing the dimensionality of the estimation problem and substantially lowering computational complexity.

Notations: In this manuscript, matrices and vectors are represented by boldface capital and lower case letters, respectively. The symbols $(\cdot)^{\mathrm{H}}$ and $(\cdot)^{\mathrm{T}}$ denote the Hermitian transpose and transpose operation of a vector or matrix. The symbol $(\cdot)^{*}$ denotes the conjugate operation and $(\cdot)^{-1}$ denotes the inverse of a square matrix. The symbol $\delta(\cdot)$ and ∇ denote the Dirac delta function and the gradient operator, respectively. $\mathrm{tr}(\cdot)$ represents the trace of a matrix.

II. SYSTEM MODEL

A. OTFS Modulation & Demodulation

As illustrated in Fig.1, we consider a single-input single-output (SISO) OTFS system architecture. To facilitate the subsequent derivations, we follow the notations in [10], where the time-frequency (TF) domain is discretized into a lattice $\mathrm{G}^{\mathrm{TF}}=\{nT_{\mathrm{sym}}, m\Delta f\}$ with sampling intervals of T_{sym} seconds in time and Δf Hz in frequency, where $n=0,\ldots,N-1$,

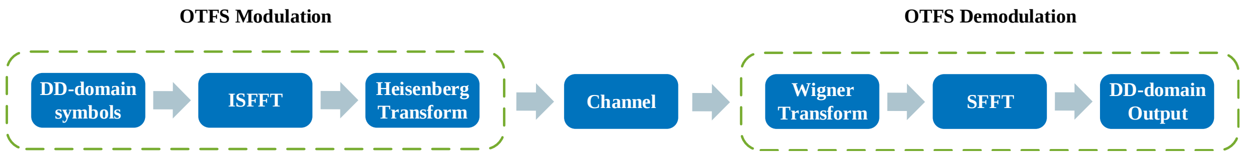

Fig. 1. Illustration of OTFS modulation and demodulation.

$m = 0, \ldots, M-1$, $N, M \in \mathbb{Z}^+$. Similarly, the delay-Doppler (DD) domain is discretized into a lattice $\mathrm{G}^{\mathrm{DD}} = \{k/NT_{\mathrm{sym}}, l/M\Delta f\}$, where $1/M\Delta f$ and $1/NT_{\mathrm{sym}}$ represent the resolutions along the delay and Doppler axes, respectively. The index ranges are given by $k = -N/2, \ldots, N/2$ and $l = 0, \ldots, M-1$.

The OTFS modulator maps DD-domain symbols $X^{\mathrm{DD}}[k,l]$ into the TF-domain symbols $X^{\mathrm{TF}}[n,m]$ using the inverse symplectic finite Fourier transform (ISFFT), which is expressed as:

$$X^{\mathrm{TF}}[n,m] = \frac{1}{\sqrt{NM}} \sum_{k=-N/2}^{N/2} \sum_{l=0}^{M-1} X^{\mathrm{DD}}[k,l] e^{-j2\pi\left(\frac{ml}{M} - \frac{nk}{N}\right)}. \tag{1}$$

Subsequently, with a rectangular pulse-shaping filter $g_{\mathrm{tx}}(t)$, the TF-domain symbols $X^{\mathrm{TF}}[n,m]$ are converted to the time-domain signal $s(t)$ through an OFDM modulator, which can be expressed as follows:

$$\begin{aligned} s(t) = & \sum_{m=0}^{M-1} \sum_{n=0}^{N-1} X^{\mathrm{TF}}[n,m] e^{j2\pi m\Delta f\left(t - \frac{M_{\mathrm{CP}}T}{M} - nT_{\mathrm{sym}}\right)} \\ & \times g_{\mathrm{tx}}(t - nT_{\mathrm{sym}}), \end{aligned} \tag{2}$$

where M_{CP} represents the length of circular prefix (CP), T denotes the time duration of an OFDM symbol excluding CP, and the pulse $g_{\mathrm{tx}}(t)$ is defined as $g_{\mathrm{tx}}(x) = 1/\sqrt{T}, 0 \leq t \leq T_{\mathrm{sym}}$.

The signal $s(t)$ is then transmitted over a time-variant wireless channel. The received signal can be expressed as

$$r(t) = \iint h(\tau, \upsilon) e^{j2\pi\upsilon(t-\tau)} s(t-\tau) d\tau d\upsilon + z(t), \tag{3}$$

where $h(\tau, \upsilon)$ represents the DD-domain channel response characterized by a delay τ and Doppler shift υ, $z(t)$ is the additive white Gaussian noise (AWGN) with variance σ^2. Due to the limited number of significant reflectors between the transmitter and receiver, the time-variant channel $h(\tau, \upsilon)$ can be modeled as a sparse sum of discrete components [10], which can be expressed as follows:

$$h(\tau, \upsilon) = \sum_{i=0}^{P-1} h_i \delta(\tau - \tau_i) \delta(\upsilon - \upsilon_i), \tag{4}$$

where P denotes the number of channel paths, $h_i \in \mathbb{C}$ is the complex channel tap coefficient of the i-th path, $\tau_i \in [0, \tau_{\max}]$ and $\upsilon_i \in [-\upsilon_{\max}, \upsilon_{\max}]$ represent the delay and Doppler shift of the i-th path, respectively. The delay and Doppler taps for the i-th path are defined as $\tau_i = l_{\tau_i}/M\Delta f$ and $\upsilon_i = k_{\upsilon_i}/NT_{\mathrm{sym}}$, where $l_{\tau_i} \in \mathbb{R}$ and $k_{\upsilon_i} \in \mathbb{R}$ represent the normalized delay and Doppler indices, respectively.

At the receiver side, after cyclic prefix removal, the received signal is transformed into the TF domain using the Wigner transform, followed by conversion to the DD domain via the symplectic finite Fourier transform (SFFT).

The end-to-end input-output relationship of the OTFS system in the DD domain is described by:

$$\begin{aligned} & Y^{\mathrm{DD}}[k,l] \\ & = \sum_{l'=0}^{M-1} \sum_{k'=-N/2}^{N/2} H_{k,l}^{\mathrm{DD}}[k',l'] X^{\mathrm{DD}}[k',l'] + z^{\mathrm{DD}}[k,l], \end{aligned} \tag{5}$$

where $H_{k,l}^{\mathrm{DD}}[k',l']$ denotes the effective DD-domain channel response, expressed as:

$$\begin{aligned} & H_{k,l}^{\mathrm{DD}}[k',l'] \\ & = \sum_{i=0}^{P-1} h(l_{\tau_i}, k_{\upsilon_i}) \Theta_N(k - k' - k_{\upsilon_i}) \Theta_M(-(l - l' - l_{\tau_i})) \\ & \quad \times \exp\left(\frac{j2\pi k_{\upsilon_i}(l - l_{\tau_i} + M_{\mathrm{CP}})}{N(M + M_{\mathrm{CP}})}\right), \end{aligned} \tag{6}$$

with the functions $\Theta_N(x) = 1/N \sum_{q=0}^{N-1} e^{-j2\pi xq/N}$ and $\Theta_M(x) = 1/M \sum_{q=0}^{M-1} e^{-j2\pi xq/M}$ capturing the effects of Doppler and delay leakage. A detailed derivation is provided in Appendix A. Notably, this input-output model accounts for fractional Doppler and delay components, making it applicable to practical scenarios.

B. OTFS Channel Estimation Model

For a typical doubly dispersive channel, it is assumed that the maximum multipath delay and Doppler shift of the channel can be represented by integer taps $l_{\tau,\max}$ and $k_{\upsilon,\max}$, where $l_{\tau,\max} < M_{\mathrm{CP}}$ and $|k_{\upsilon,\max}| \ll N$. Given that the positions of the delay and Doppler shift of the channel are initially unknown, a widely adopted strategy is to predefine a set of grids over the delay and Doppler domains, upon which the sensing matrix is subsequently constructed. However, the resolution of the DD-domain channel is intrinsically determined by the system parameters $M, \Delta f, N$ and T_{sym}. Due to limitations imposed by the pulse duration and bandwidth of OTFS, the inherent DD-domain grid G^{DD} is insufficient to provide a sparse representation of the channel. Thus, we define virtual grids with higher resolution in both the delay and Doppler domains. Under uniform sampling, the virtual delay and Doppler grids are respectively denoted as $\mathbf{l}_{\mathrm{vir}} = [l_{\mathrm{vir},0}, \ldots, l_{\tau}, \ldots, l_{\mathrm{vir},L_\tau - 1}]^{\mathrm{T}} \in \mathbb{R}^{L_\tau \times 1}$ and $\mathbf{k}_{\mathrm{vir}} = [k_{\mathrm{vir},0}, \ldots, k_{\upsilon}, \ldots, k_{\mathrm{vir},L_\upsilon - 1}]^{\mathrm{T}} \in \mathbb{R}^{L_\upsilon \times 1}$, with resolutions $r_\tau = l_{\tau,\max}/(L_\tau - 1)$ and $r_\upsilon = (2k_{\upsilon,\max})/(L_\upsilon - 1)$. Based on the predefined virtual grids, the sensing matrix

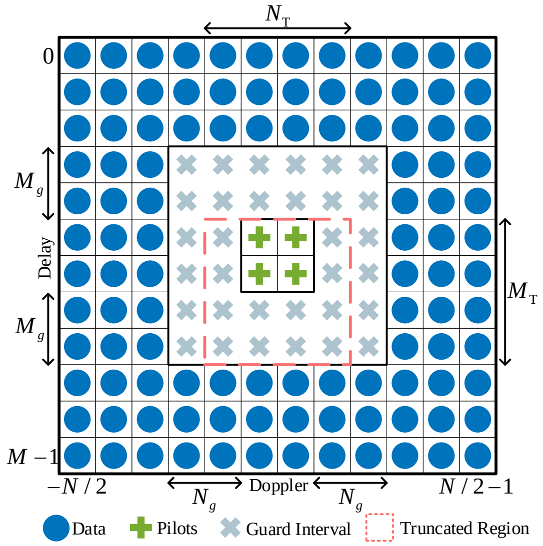

Fig. 2. The arrangement of data, pilot and guard interval in an OTFS frame.

$\mathbf{\Phi}(\mathbf{l}_\mathrm{vir}, \mathbf{k}_\mathrm{vir}) \in \mathcal{C}^{MN\times L_\tau L_\upsilon}$ is constructed. Consequently, the channel estimation model can be represented in a vector form as follows:

$$\mathbf{y}^\mathrm{DD} = \mathbf{\Phi}(\mathbf{l}_\mathrm{vir}, \mathbf{k}_\mathrm{vir})\mathbf{h} + \mathbf{z}^\mathrm{DD}, \tag{7}$$

where $\mathbf{h} \in \mathbb{C}^{L_\tau L_\upsilon \times 1}$ represents the channel gains. The $(lN + k, l_\tau L_\upsilon + k_\upsilon)$-th element in $\mathbf{\Phi}(\mathbf{l}_\mathrm{vir}, \mathbf{k}_\mathrm{vir})$ is given by

$$\phi(l_\tau, k_\upsilon)_{l,k} = \sum_{l'=0}^{M-1} \sum_{k'=-N/2}^{N/2-1} X^\mathrm{DD}[k', l'] e^{j2\pi \frac{(l-l_\tau+M_\mathrm{CP})k_\upsilon}{(M+M_\mathrm{CP})N}} \times \Theta_N(k - k' - k_\upsilon)\Theta_M(-(l - l' - l_\tau)). \tag{8}$$

To obtain the channel impulsive response, the known reference symbols must be inserted as pilots in the OTFS frame. As shown in Fig. 2, pilots are placed at the center of an OTFS frame. The positions of pilots are denoted as $k = k_{\mathrm{p}_0}, k_{\mathrm{p}_1}, \cdots k_{\mathrm{p}_{N_\mathrm{p}-1}}$ and $l = l_{\mathrm{p}_0}, l_{\mathrm{p}_1}, \cdots l_{\mathrm{p}_{M_\mathrm{p}-1}}$, where M_P and N_P represent the lengths of the pilots along delay and Doppler axes, respectively. In order to eliminate the interference between data and pilots, the guard intervals are required and placed between them. As stated in [12], the guard intervals should be set to $M_\mathrm{g} \geq l_{\tau,\max}$ along the delay dimension and $N_\mathrm{g} \geq 2k_{\upsilon,\max}$ along the Doppler dimension. Since the channel in the DD domain is finite, only a specific portion of the receiver is influenced by the pilot symbols. As a result, the region affected by the pilot symbols will be extracted from the received signal for channel estimation. The truncated region is within the range $k_{\mathrm{p}_0} - k_{\upsilon,\max} \leq k \leq k_{\mathrm{p}_{N_\mathrm{p}-1}} + k_{\upsilon,\max}$ and $l_{\mathrm{p}_0} \leq l \leq l_{\mathrm{p}_{M_\mathrm{p}-1}} + l_{\tau,\max}$ with $M_\mathrm{T} = M_\mathrm{p} + l_{\tau,\max}$ and $N_\mathrm{T} = N_\mathrm{p} + 2k_{\upsilon,\max}$. As a result, the extracted receiving signal can be expressed as

$$\mathbf{y}_\mathrm{T}^\mathrm{DD} = \mathbf{\Phi}_\mathrm{T}(\mathbf{l}_\mathrm{vir}, \mathbf{k}_\mathrm{vir})\mathbf{h} + \mathbf{z}_\mathrm{T}^\mathrm{DD}, \tag{9}$$

where $\mathbf{y}_\mathrm{T}^\mathrm{DD} \in \mathbb{C}^{M_\mathrm{T} N_\mathrm{T} \times 1}$ is the extracted received signal, $\mathbf{z}_\mathrm{T}^\mathrm{DD} \in \mathbb{C}^{M_\mathrm{T} N_\mathrm{T} \times 1}$ denotes the noise and $\mathbf{\Phi}_\mathrm{T}(\mathbf{l}_\mathrm{vir}, \mathbf{k}_\mathrm{vir}) \in \mathbb{C}^{M_\mathrm{T} N_\mathrm{T} \times L_\tau L_\upsilon}$ represents the truncated sensing matrix. This formulation provides a 1D channel estimation model for the OTFS system.

C. Bayesian Learning Framework

Due to the sparsity of the channel in the DD domain, OTFS channel estimation can be formulated as a sparse signal recovery (SSR) problem. Given the superior performance of Bayesian learning-based methods in sparse recovery, we adopt a Bayesian learning approach to design the channel estimation algorithm, and provide a brief overview here.

In SBL framework, it is assumed that all the elements in $\mathbf{y}_\mathrm{T}^\mathrm{DD}$ are mutually independent. The likelihood function is therefore expressed as

$$p(\mathbf{y}_\mathrm{T}^\mathrm{DD} | \mathbf{h}, \alpha) = \mathcal{CN}(\mathbf{y}_\mathrm{T}^\mathrm{DD} | \mathbf{\Phi}_\mathrm{T}\mathbf{h}, \alpha^{-1}\mathbf{I}), \tag{10}$$

where $\alpha = \sigma^{-2}$ denotes the noise precision. We assume that $\mathbf{h}$ follows a zero-mean complex Gaussian distribution as follows

$$p(\mathbf{h}|\boldsymbol{\gamma}) = \mathcal{CN}(\mathbf{h}|\mathbf{0}, \mathrm{diag}(\boldsymbol{\gamma}^{-1})), \tag{11}$$

where $\boldsymbol{\gamma}$ denotes the precision vector $[\gamma_0, \gamma_1, \cdots, \gamma_{L_\tau L_\upsilon - 1}]^\mathrm{T}$ with $\gamma_j, j = 0, 1, \cdots, L_\tau L_\upsilon - 1$, as independent hyper-parameters that control the strength of prior. In addition, a Gamma prior is imposed on each value of $\boldsymbol{\gamma}$ and α as

$$p(\boldsymbol{\gamma}) = \prod_{j=0}^{L_\tau L_\upsilon - 1} \mathrm{Gamma}(\gamma_j; a, b), \tag{12}$$

$$p(\alpha) = \mathrm{Gamma}(\alpha; c, d). \tag{13}$$

Given the prior and likelihood function, the posterior distribution of can be expressed as

$$p(\mathbf{h}|\mathbf{y}_\mathrm{T}^\mathrm{DD}, \boldsymbol{\gamma}, \alpha) = \mathcal{CN}(\mathbf{h}|\boldsymbol{\mu}, \mathbf{\Sigma}), \tag{14}$$

where

$$\boldsymbol{\mu} = \alpha \mathbf{\Sigma} (\mathbf{\Phi}_\mathrm{T})^\mathrm{H} \mathbf{y}_\mathrm{T}^\mathrm{DD}, \tag{15}$$

$$\mathbf{\Sigma} = (\alpha (\mathbf{\Phi}_\mathrm{T})^\mathrm{H} \mathbf{\Phi}_\mathrm{T} + \mathrm{diag}(\boldsymbol{\gamma}))^{-1}. \tag{16}$$

To update the hyper-parameters iteratively, we maximize their posterior distribution as follows

$$\{\hat{\boldsymbol{\gamma}}, \hat{\alpha}\} \propto \arg\max \ \ln p(\mathbf{y}_\mathrm{T}^\mathrm{DD}, \boldsymbol{\gamma}, \alpha). \tag{17}$$

In order to maximize the joint probability density, an expectation maximization (EM) strategy is employed. The hyper-parameters can be updated as follows.

$$\hat{\gamma}_j = \frac{a + 1}{b + \mu_j^2 + \mathbf{\Sigma}_{jj}}, \tag{18}$$

$$\hat{\alpha} = \frac{M_\mathrm{T} N_\mathrm{T} + c}{\|\mathbf{y}_\mathrm{T}^\mathrm{DD} - \mathbf{\Phi}_\mathrm{T}\boldsymbol{\mu}\|_2^2 + \mathrm{tr}(\mathbf{\Phi}_\mathrm{T} \mathbf{\Sigma} \mathbf{\Phi}_\mathrm{T}^\mathrm{H}) + d}, \tag{19}$$

where $\mathbf{\Sigma}_{jj}$ represents the $(j+1)$-th diagonal element in $\mathbf{\Sigma}$ and μ_j is the $(j+1)$-th element in $\boldsymbol{\mu}$.

Although SBL is a high-performance SSR algorithm, it has certain limitations when applied to OTFS channel estimation. Firstly, the delay and Doppler domains typically exhibit different sparse patterns. Nevertheless, SBL, as a 1D on-grid SSR algorithm, can not fully exploit these characteristics. Secondly, while finer virtual grids can result in a sparser channel representation, the dimensionality of the model is also be increased significantly, thereby raising the computational complexity. Finally, since the sensing matrix in SBL is constructed with predefined sampling points, it struggles to mitigate the effects of fractional delay and Doppler shifts.

III. DECOUPLED CHANNEL ESTIMATION FRAMEWORK

In this section, to fully exploit the channel characteristics in the delay and Doppler domains, we propose a decoupled channel estimation framework which separates the originally DD-domain channel into the delay and Doppler domain components for more effective estimation. For clarity and brevity, the main variables and notations used in Sections III and IV are summarized in Table I.

TABLE I
MAIN NOTATIONS IN SECTION III AND IV

Notation	Description
$\mathbf{\Phi}_\tau$	Delay-domain sensing matrix
$\mathbf{\Phi}_\upsilon$	Doppler-domain sensing matrix
$\mathbf{h}_\tau$	Delay-domain CIR
$\mathbf{h}_{\upsilon_1}$	CIR of the first Doppler estimation
$\mathbf{h}_{\upsilon_1}$	CIR of the second Doppler estimation
$\mathcal{S}$	Doppler sub-band set
L_{seg}	Number of Doppler segments during delay estimation
$\mathcal{T}$	Subset of $\mathbf{l}_{\text{vir}}$
$\mathcal{T}_{\text{sel}}$	Selected delay indices set
$\mathbf{l}_{\tau s}$	Selected delay indices vector
$l_{\tau s}$	A generic element of $\mathbf{l}_{\tau s}$
$\mathcal{R}_1, \mathcal{R}_2$	Doppler sub-band sets for sensing matrix construction
$\mathcal{R}_s^1, \mathcal{R}_s^2$	Selected Doppler sub-band sets
$L_{\text{b}_1}, L_{\text{b}_2}$	Number of Doppler segments during Doppler estimation
$\mathcal{I}_1, \mathcal{I}_2$	Selected Doppler sub-band indices sets

To begin with, we consider only the case of integer delay taps. With sufficiently large system bandwidth, the delay resolution is adequate to map each path delay onto an integer normalized delay tap, thereby eliminating the need to account for fractional delays. Since there is no impact from fractional delays, the virtual delay-domain resolution can be set to $r_\tau = 1$. In the conventional 1D channel estimation model, the channel is modeled as a 1D vector, where each delay tap corresponds to L_υ Doppler shift sampling points. Unlike the conventional model, a piecewise integration is conducted over the Doppler domain. Then, we construct a delay-domain sensing matrix $\mathbf{\Phi}_\tau(\mathbf{l}_{\text{vir}}, \mathcal{S}(i_\tau)) \in \mathbb{C}^{M_{\text{T}}N_{\text{T}} \times L_\tau L_{\text{seg}}}$, which depends solely on the normalized delay l_τ. The $(lN_{\text{T}}+k, l_\tau L_{\text{seg}}+i_\tau)$-th element of $\mathbf{\Phi}_\tau(\mathbf{l}_{\text{vir}}, \mathcal{S}(i_\tau))$ can be expressed as

$$\begin{aligned} \mathbf{\Phi}_\tau(lN_{\text{T}} + k, l_\tau L_{\text{seg}} + i_\tau) &= \int_{\mathcal{S}(i_\tau)} \phi(l_\tau, \nu)_{l,k} d\nu \\ = \int_{\mathcal{S}(i_\tau)} \sum_{l'=0}^{M-1} \sum_{k'=-N/2}^{N/2} & X^{\text{DD}}[k', l'] e^{j\frac{2\pi}{N}\eta_\tau \nu} \\ \times \Theta_N(k - k' - \nu)&\Theta_M(-(l - l' - l_\tau))d\nu, \end{aligned} \tag{20}$$

where $\eta_\tau = (l - l_\tau + M_{\text{CP}})/(M + M_{\text{CP}})$ and ν represents a continuous random variable in the Doppler domain. The Doppler-domain region $[-k_{\upsilon,\max}, k_{\upsilon,\max}]$ is divided into L_{seg} segments ($L_{\text{seg}} \geq 1$), with each segment denoted as $\mathcal{S}(i_\tau), i_\tau = 1, \ldots, L_{\text{seg}}$. When multi-segment integration over the Doppler domain is performed, the correlation between atoms in the sensing matrix is reduced, leading to improved system stability and enhanced delay estimation performance. See the Appendix B for the detailed derivation of (20).

By employing the delay-domain sensing matrix, the original DD-domain channel is decoupled into delay-domain channel. Similar to the model in (9), delay estimation can be described as a 1D on-grid SSR problem as follows

$$\mathbf{y}_{\text{T}}^{\text{DD}} = \mathbf{\Phi}_\tau(\mathbf{l}_{\text{vir}}, \mathcal{S}(i_\tau))\mathbf{h}_\tau + \mathbf{z}_{\text{T}}^{\text{DD}}, \tag{21}$$

where $\mathbf{h}_\tau \in \mathbb{C}^{L_\tau L_{\text{seg}} \times 1}$ represents the delay-domain channel with total power $\|\mathbf{h}_\tau\|_2^2$. It is important to emphasize that $\mathbf{h}_\tau$ encapsulates solely the delay characteristics of the original channel $\mathbf{h}$ in (9), rather than being directly derived from $\mathbf{h}$.

The delay-domain channel can be estimated by any 1D SSR or block SSR method. Based on the results, the delay taps can be identified and selected for subsequent Doppler shifts and channel gain estimation, subject to the following condition

$$\mathcal{T}_{\text{sel}} = \underset{\mathcal{T} \subseteq \mathbf{l}_{\text{vir}}}{\arg\min} |\mathcal{T}| \text{ s.t. } \frac{\sum_{l_\tau \in \mathcal{T}} \sum_{i_\tau=1}^{L_{\text{seg}}} |h_{\tau, l_\tau + i_\tau}|^2}{\|\mathbf{h}_\tau\|_2^2} \geq \epsilon_\tau. \tag{22}$$

where $l_\tau \in \mathbf{l}_{\text{vir}}$, ϵ_τ is the threshold for selecting delay taps, and $\mathcal{T}_{\text{sel}}$ denotes the set of selected indices of $\mathbf{l}_{\text{vir}}$. The unselected elements are ignored, reducing the dimensionality of the subsequent estimation model and thereby decreasing computational complexity. We denote the vector of the selected delay taps as $\mathbf{l}_{\tau s} = [l_{\tau s,0}, l_{\tau s,1}, \ldots, l_{\tau s,L_s-1}]^{\text{T}} \in \mathbb{Z}^{L_s \times 1}$, where L_s is the length of $\mathbf{l}_{\tau s}$. Once the delay taps are determined, they are substituted into (9) as follows

$$\mathbf{y}_{\text{T}}^{\text{DD}} = \mathbf{\Phi}_{\text{T}}(\mathbf{l}_{\tau s}, \mathbf{k}_{\text{vir}})\mathbf{h}_\upsilon + \mathbf{z}_{\text{T}}^{\text{DD}}, \tag{23}$$

where $\mathbf{h}_\upsilon \in \mathbb{C}^{L_s L_\upsilon \times 1}$ represents the Doppler-domain channel. At this point, the original DD-domain channel has been successfully decoupled into separate delay and Doppler domains for individual estimation.

When dealing with a bandwidth-limited OTFS system, the delay-domain resolution $1/M\Delta f$ significantly decreases, requiring consideration of the impact of fractional delays. To better characterize fractional delays, delay-domain virtual grids with higher resolution are employed, i.e., $r_\tau < 1$.

To enhance the robustness of the algorithm, the two points at both ends of the selected delay tap are extracted as well. The unselected elements are ignored. The selected delay taps are also denoted as $\mathbf{l}_{\tau s} = [l_{\tau s,0}, l_{\tau s,1}, \cdots, l_{\tau s,L_s-1}]^{\text{T}} \in \mathbb{Z}^{L_s \times 1}$.

In delay estimation, both the threshold parameter ϵ_τ and the number of Doppler-domain segments L_{seg} influence performance. Their impact on the system will be discussed in the simulation results.

IV. DECOUPLED BAYESIAN LEARNING CHANNEL ESTIMATION

In this section, we develop a DC-BL algorithm for channel estimation, designed to reconstruct the sparse channel in the DD domain with the proposed decoupled channel estimation framework. We also discuss the performance of the approach and analyze its convergence.

A. Decoupled Bayesian Learning Channel Estimation

To efficiently reconstruct the DD-domain channel, we develop a channel estimation algorithm based on DC-BL. The algorithm exploits the distinct sparsity patterns in the delay and Doppler domains and achieves super-resolution channel estimation while maintaining relatively low computational complexity.

First, we consider the case of integer delays. The corresponding r_τ is set to 1. Based on the estimation model established in (21), delay estimation is performed. When $L_{\mathrm{seg}} = 1$, SBL is applied for delay estimation. For $L_{\mathrm{seg}} > 1$, block sparse Bayesian learning (BSBL) is employed. Following [26], the update rules in (16), (18) and (19) are accordingly modified. Specifically, (16) is modified as

$$\boldsymbol{\Sigma} = (\alpha(\boldsymbol{\Phi}_{\mathrm{T}})^{\mathrm{H}}\boldsymbol{\Phi}_{\mathrm{T}} + \boldsymbol{\Sigma}_{\mathbf{B}}^{-1})^{-1}, \tag{24}$$

where $\boldsymbol{\Sigma}_{\mathbf{B}} = \mathrm{diag}(\gamma_0^{-1}\mathbf{B}_0, \ldots, \gamma_{l_{\tau,\max}}^{-1}\mathbf{B}_{l_{\tau,\max}})$. $\mathbf{B}_j, j = 0, 1, \ldots, L_\tau - 1$, is a positive definite matrix that captures intra-block correlation structure. The covariance matrix $\mathbf{B}_j$ is updated as

$$\mathbf{B}_j = \gamma_j(\boldsymbol{\Sigma}_j + \mu_j(\mu_j)^{\mathrm{H}}), \tag{25}$$

where $\boldsymbol{\Sigma}_j = \boldsymbol{\Sigma}(jL_{\mathrm{seg}}+1 : (j+1)L_{\mathrm{seg}}, jL_{\mathrm{seg}}+1 : (j+1)L_{\mathrm{seg}})$ and $\boldsymbol{\mu}_j = \boldsymbol{\mu}(jL_{\mathrm{seg}}+1 : (j+1)L_{\mathrm{seg}})$.

Furthermore, (19) is modified as

$$\hat{\gamma}_j = \frac{L_{\mathrm{seg}}}{\mathrm{tr}(\mathbf{B}_j^{-1}(\boldsymbol{\Sigma}_j + \mu_j(\mu_j)^{\mathrm{H}}))}. \tag{26}$$

Next, we focus on the Doppler-domain channel estimation. While virtual grids with high resolution can improve the sparse representation of the channel, increasing the number of virtual grids indefinitely would impose a significant computational burden on the system. To effectively manage the unavoidable fractional Doppler shifts, we devise a super-resolution Bayesian learning method for Doppler-domain channel estimation with specifically designed sensing matrix. Based on the virtual grids defined in $\mathbf{k}_{\mathrm{vir}}$, the region within the maximum Doppler shift $|k_{\upsilon,\max}|$ is divided into L_{b_1} parts. In light of the previously estimated delay taps, the regions for Doppler-domain channel estimation can be represented as $\boldsymbol{\mathcal{R}}_1 = \{\mathcal{R} : R_1(k_{b_1}, l_{\tau s}) \leq \mathcal{R} \leq R_1(k_{b_1}, l_{\tau s}) + \Delta_1, R_1(k_{b_1}, l_{\tau s}) = (l_{\tau s}L_{b_1} + k_{b_1})\Delta_1, k_{b_1} = 0, \cdots, L_{b_1} - 1\}$, where $\Delta_1 = 2k_{\upsilon,\max}/L_{b_1}$ indicates the size of each segment. By integrating these L_{b_1} regions, each column of the sensing matrix is formed by aggregating the Doppler shifts within the specified region. This approach ensures that the true Doppler shifts are captured within the sensing matrix, thereby mitigating the effects of energy leakage.

Thus, the sensing matrix $\boldsymbol{\Phi}_\upsilon(\boldsymbol{\mathcal{R}}_1) \in \mathbb{C}^{M_{\mathrm{T}}N_{\mathrm{T}} \times L_s L_{b_1}}$ for Doppler-domain channel estimation can be constructed as

$$\begin{aligned}\boldsymbol{\Phi}_\upsilon(\boldsymbol{\mathcal{R}}_1) = [&\boldsymbol{\phi}_\upsilon(R_1(0, l_{\tau s,0})), \boldsymbol{\phi}_\upsilon(R_1(1, l_{\tau s,0})), \cdots, \\ &\boldsymbol{\phi}_\upsilon(R_1(k_{b_1}, l_{\tau s,i_s})), \cdots, \boldsymbol{\phi}_\upsilon(R_1(L_{b_1} - 1, l_{\tau s,L_s-1}))],\end{aligned} \tag{27}$$

where $i_s = 0, 1, \cdots, L_s - 1$. The $(lN_{\mathrm{T}} + k)$-th element of $\boldsymbol{\phi}_\upsilon(R_1(k_{b_1}, l_{\tau s,i_s}))$ can be denoted as [27]

$$\begin{aligned}&\phi_\upsilon(R_1(k_{b_1}, l_{\tau s,i_s}))_{lN_{\mathrm{T}}+k} \\ &= \int_{k_{b_1}\Delta_1}^{(k_{b_1}+1)\Delta_1} \sum_{l'=0}^{M-1} \sum_{k'=-N/2}^{N/2} X^{\mathrm{DD}}[k', l'] e^{j\frac{2\pi}{N}\eta_\tau \nu} \\ &\quad \times \Theta_N(k - k' - \nu)\Theta_M(-(l - l' - l_{\tau s,i_s}))d\nu,\end{aligned} \tag{28}$$

where $l_{\tau s,i_s}$ denotes the i_s-th element in $\mathbf{l}_{\tau s}$.

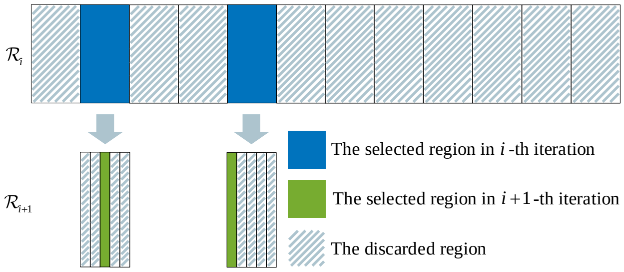

Fig. 3. The iterative update process of sensing matrix construction for Doppler-domain channel estimation.

Based on the sensing matrix in (27), Doppler-domain channel estimation can be formulated as a 1D SSR problem as

$$\mathbf{y}_{\mathrm{T}}^{\mathrm{DD}} = \boldsymbol{\Phi}_\upsilon(\boldsymbol{\mathcal{R}}_1)\mathbf{h}_{\upsilon_1} + \mathbf{z}_{\mathrm{T}}^{\mathrm{DD}}, \tag{29}$$

where $\mathbf{h}_{\upsilon_1} \in \mathbb{C}^{L_s L_{b_1} \times 1}$ represents the Doppler-domain CIR, which can also be estimated through SBL. Founded on the estimation result $\mathbf{h}_{\upsilon_1}$, the index of the region containing the true Doppler-domain channel taps is determined by the criterion

$$(l_{\tau s}L_{b_1} + k_{b_1})_{\mathrm{sel}} = \arg \max_{l_{\tau s}L_{b_1} + k_{b_1}} |\mathbf{h}_{\upsilon_1}(l_{\tau s}L_{b_1} + k_{b_1})|. \tag{30}$$

For robustness, both the neighboring indices are included, resulting in the selected indices being defined as $\boldsymbol{\mathcal{I}}_1 = \{(k'_{b_1}, l_{\tau s}) : k'_{b_1} \in \{k_{b_1-1}, k_{b_1}, k_{b_1+1}\}, l_{\tau s}L_{b_1} + k_{b_1} = (l_{\tau s}L_{b_1} + k_{b_1})_{\mathrm{sel}}\}$. The selected region can then be described as $\boldsymbol{\mathcal{R}}_s^1 = \{\mathcal{R} : R_s^1(k_{b_1}, l_{\tau s}) \leq \mathcal{R} \leq R_s^1(k_{b_1}, l_{\tau s}) + \Delta_1, R_s^1(k_{b_1}, l_{\tau s}) = (l_{\tau s}L_{b_1} + k_{b_1})\Delta_1, (k_{b_1}, l_{\tau s}) \in \boldsymbol{\mathcal{I}}_1\}$. In contrast, the unselected areas are discarded. As shown in Fig.3, to further enhance the performance of channel estimation in the Doppler domain, each selected region can be subdivided into L_{b_2} smaller regions. Accordingly, the region for Doppler-domain channel estimation is then denoted as $\boldsymbol{\mathcal{R}}_2 = \{\mathcal{R} : R_2(k_{b_2}, l_{\tau s}) \leq \mathcal{R} \leq R_2(k_{b_2}, l_{\tau s}) + \Delta_2, R_2(k_{b_2}, l_{\tau s}) = R_s^1(k_{b_1}, l_{\tau s}) + k_{b_2}\Delta_2, k_{b_2} = 0, 1, \cdots, L_{b_2} - 1\}$, where $\Delta_2 = 3\Delta_1/L_{b_2}$. With the further divided regions in the Doppler domain, a more refined sensing matrix is constructed as follows

$$\begin{aligned}\boldsymbol{\Phi}_\upsilon(\boldsymbol{\mathcal{R}}_2) = [&\boldsymbol{\phi}_\upsilon(R_2(0, l_{\tau s,0})), \boldsymbol{\phi}_\upsilon(R_2(1, l_{\tau s,0})), \cdots, \\ &\boldsymbol{\phi}_\upsilon(R_2(k_{b_2}, l_{\tau s,i_s})), \cdots, \boldsymbol{\phi}_\upsilon(R_2(L_{b_2} - 1, l_{\tau s,L_s-1}))].\end{aligned} \tag{31}$$

where the $(lN_{\mathrm{T}} + k)$-th element of $\boldsymbol{\phi}_\upsilon(R_2(k_{b_2}, l_{\tau s,i_s}))$ can be represented similarly to (28), and will not be repeated here.

With the newly constructed sensing matrix in (31), the channel estimation model in (27) can be transformed into

$$\mathbf{y}_{\mathrm{T}}^{\mathrm{DD}} = \boldsymbol{\Phi}_\upsilon(\boldsymbol{\mathcal{R}}_2)\mathbf{h}_{\upsilon_2} + \mathbf{z}_{\mathrm{T}}^{\mathrm{DD}}, \tag{32}$$

where $\mathbf{h}_{\upsilon_2} \in \mathbb{C}^{3L_s L_{b_2} \times 1}$ denotes the Doppler-domain CIR corresponding to the newly constructed sensing matrix $\boldsymbol{\Phi}_\upsilon(\boldsymbol{\mathcal{R}}_2)$. Also, the selected indices and regions could be similarly defined as $\boldsymbol{\mathcal{I}}_2$ and $\boldsymbol{\mathcal{R}}_s^2$, respectively, following the approach described earlier. Since the sensing matrix $\boldsymbol{\Phi}_\upsilon(\boldsymbol{\mathcal{R}}_2)$ incorporates virtual grids with higher resolution in the Doppler domain, the performance of channel estimation is further enhanced

Algorithm 1 DC-BL Algorithm

```
Input: the truncated receiving signal $\mathbf{y}_{\mathrm{T}}^{\mathrm{DD}}$, the delay-domain sensing matrix $\mathbf{\Phi}_{\tau}(\mathbf{l}_{\tau}, \mathcal{S}(i_{\tau}))$, the threshold $\epsilon_{\tau}$, $\epsilon_{\mathrm{END}}$, the maximum iteration $k_{\max}$, the number of separations $I_{\mathrm{Sep}}$.
    Delay-domain channel estimation:
 1: Initialization: Channel precision $\gamma_{\tau j}^{k} = 1, \forall j$ , the noise precision $\alpha_{\tau}^{k} > 0$ and the counter $k = 1$.
 2: repeat
 3:     Calculate $\boldsymbol{\mu}_{\tau}^{k}$ and $\mathbf{\Sigma}_{\tau}^{k}$ by (15) and (16)($L_{\mathrm{seg}} = 1$)/(24)($L_{\mathrm{seg}} > 1$)
 4:     Update $\boldsymbol{\gamma}_{\tau}^{k+1}$ and $\alpha_{\tau}^{k+1}$ by (26) and (19)
 5: until $\|\boldsymbol{\mu}_{\tau}^{k+1} - \boldsymbol{\mu}_{\tau}^{k}\|_2^2 \le \epsilon_{\mathrm{END}}$ or $k = k_{\max}$
 6: The selected delay taps are denoted as $\mathbf{l}_{\tau s}$
    Doppler-domain channel estimation:
 7: for $i = 1$ to $I_{\mathrm{Sep}}$ do
 8:     Set the number of bands, $L_{b_i}$
 9:     Construct the sensing matrix $\mathbf{\Phi}_{\upsilon}(\boldsymbol{\mathcal{R}}_i)$
10:     Initialization: Channel precision $\gamma_{\upsilon j}^{k} = 1, \forall j$ , the noise precision $\alpha_{\upsilon}^{k} > 0$ and counter $k = 1$.
11:     repeat
12:         Calculate $\boldsymbol{\mu}_{\upsilon}^{k}$ and $\mathbf{\Sigma}_{\upsilon}^{k}$ by (15) and (16)
13:         Update $\boldsymbol{\gamma}_{\upsilon}^{k+1}$ and $\alpha_{\upsilon}^{k+1}$ by (18) and (19)
14:     until $\|\boldsymbol{\mu}_{\upsilon}^{k+1} - \boldsymbol{\mu}_{\upsilon}^{k}\|_2^2 \le \epsilon_{\mathrm{END}}$ or $k = k_{\max}$
15:     Select the region index $\boldsymbol{\mathcal{I}}_i$ according to (30)
16:     Update the selected region as $\boldsymbol{\mathcal{R}}_s^{i}$
17: end for
Output: Channel gains $\boldsymbol{\mu}_{\upsilon}^{k+1}$, the selected normalized delay taps $\mathbf{l}_{\tau s}$, the selected normalized Doppler shifts $R_s^{i-1}(k_{b_{i-1}}, l_{\tau s}) + k_{b_i}\Delta_i + 1/2\Delta_i$, $(k_{b_i}, l_{\tau s}) \in \boldsymbol{\mathcal{I}}_i$
```

Algorithm 2 DC-BL Algorithm for Low Virtual-Grid Resolution in the Doppler domain

```
Input: the truncated received signal $\mathbf{y}_{\mathrm{T}}^{\mathrm{DD}}$, the delay-domain sensing matrix $\mathbf{\Phi}_{\tau}(\mathbf{l}_{\tau}, \mathcal{S}(i_{\tau}))$, the threshold $\epsilon_{\tau}$, $\epsilon_{\mathrm{END}}$, the maximum iteration $k_{\max}$, the number separations $I_{\mathrm{Sep}}$.
Delay-domain channel estimation:
Follow the steps $1-6$ in Algorithm 1 to estimate the delay-domain channel
Doppler-domain channel estimation:
Follow the steps $7-17$ in Algorithm 1 ($i = 1$) to acquire an approximate position of the Doppler shifts
Define virtual grids $\mathbf{K}_{\mathrm{vir}}^{\mathbf{l}_{\tau s}}$ with the desired resolution $\Delta_d$ and construct the sensing matrix by (33)
repeat
    Calculate $\boldsymbol{\mu}_{\upsilon}^{k}$ and $\mathbf{\Sigma}_{\upsilon}^{k}$ by (15) and (16)
    Update the hyper-parameters $\boldsymbol{\gamma}_{\upsilon}^{k+1}$, $\alpha_{\upsilon}^{k+1}$ and $\mathbf{K}_{\mathrm{vir}}^{\mathbf{l}_{\tau s},k+1}$ by (18), (19) and (38)
until $\|\boldsymbol{\mu}_{\upsilon}^{k+1} - \boldsymbol{\mu}_{\upsilon}^{k}\|_2^2 \le \epsilon_{\mathrm{END}}$ or $k = k_{\max}$
Output: Channel gains $\boldsymbol{\mu}_{\upsilon}^{k+1}$, the selected normalized delay taps $\mathbf{l}_{\tau s}$, the normalized Doppler shifts $\mathbf{K}_{\mathrm{vir}}^{\mathbf{l}_{\tau s},k+1}$
```

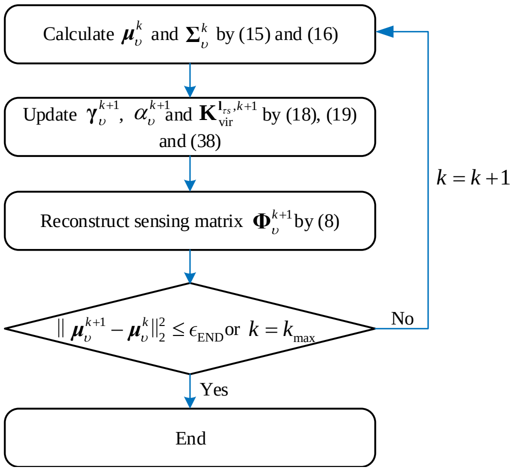

Fig. 4. Flowchart of parameter update in **Algorithm** 2

by model in (32). The above iterative update process can be repeated until a satisfactory channel resolution is achieved.

Consequently, the DD-domain channel has been estimated in delay and Doppler domains respectively by the DC-BL approach. In summary, the steps of the proposed DC-BL algorithm are summarized in **Algorithm** 1.

B. Channel Estimation based on DC-BL for Low-resolution Virtual Grids in the Doppler Domain

Although high-resolution virtual grids can provide a more accurate representation of the channel, it also significantly increases the computational complexity. This issue is particularly pronounced in low SNR scenarios, where the threshold-based tap selection method tends to introduce a large number of redundant taps, imposing a substantial burden on receivers with limited computational capabilities. Hence, computationally constrained receivers must compromise on resolution to manage complexity. The framework is adaptable, allowing for suitable methods for Doppler-domain channel estimation when dealing with low-resolution virtual grids. As grid resolution decreases, on-grid models struggle to accurately represent the Doppler-domain channel. Studies on fractional Doppler shifts show that larger shifts lead to reduced received SNR [25]. In light of the aforementioned circumstances, the virtual grids in the dictionary $\mathbf{\Phi}_{\upsilon}$ could be treated as unknown parameters. Since the normalized Doppler shifts may occur within the range $-k_{\upsilon,\max}$ to $k_{\upsilon,\max}$, each virtual grid $k_{\mathrm{vir}} \in \mathbf{k}_{\mathrm{vir}}$, when treated as an unknown parameter, is a continuous random variable. A parametric dictionary learning model is implemented for the Doppler-domain channel estimation. Then, based on this model, we propose a decoupled Bayesian channel estimation algorithm specifically for low-resolution virtual grids.

To begin with, the delay estimation is performed following the procedures outlined in **Algorithm** 1, and thus, will not be reiterated here. For the Doppler-domain channel estimation, virtual grids $\mathbf{k}_{\mathrm{vir}} \in \mathbb{R}^{L_{\upsilon} \times 1}$ are initially defined with a coarse resolution of $r_{\upsilon} > \Delta_d$, where Δ_d is the desired resolution. Subsequently, the sensing matrix is constructed as mentioned in (27). Based on the model (29) and the SBL algorithm, an approximate position of the Doppler domain channel can be determined and denoted as $\boldsymbol{\mathcal{R}}_s^{1}$.

Next, regions without Doppler-domain channel taps will be excluded, and virtual grids with the desired resolution Δ_d will be defined in the remaining regions. The virtual grids related to the selected delay tap $l_{\tau s}$ are formulated in vector form as $\mathbf{k}_{\text{vir}}^{l_{\tau s}} = [k_{\text{vir},0}^{l_{\tau s}}, k_{\text{vir},1}^{l_{\tau s}}, \cdots, k_{\text{vir},i_d}^{l_{\tau s}}, \cdots, k_{\text{vir},L_d-1}^{l_{\tau s}}]^{\text{T}} \in \mathbb{R}^{L_d \times 1}$, where $L_d = 3\Delta_1/\Delta_d + 1$ represents the length of $\mathbf{k}_{\text{vir}}^{l_{\tau s}}$.[1] With the selected delay taps and defined virtual grids, the Doppler-domain sensing matrix $\mathbf{\Phi}_{\upsilon}(\mathbf{l}_{\tau s}, \mathbf{k}_{\text{vir}}^{l_{\tau s}}) \in \mathbb{C}^{M_{\text{T}} N_{\text{T}} \times L_s L_d}$ can be constructed as follows

$$\begin{aligned}\mathbf{\Phi}_{\upsilon}(\mathbf{l}_{\tau s}, \mathbf{k}_{\text{vir}}^{l_{\tau s}}) = [&\boldsymbol{\phi}_{\upsilon}(l_{\tau s,0}, k_{\text{vir},0}^{l_{\tau s,0}}), \boldsymbol{\phi}_{\upsilon}(l_{\tau s,0}, k_{\text{vir},1}^{l_{\tau s,0}}), \cdots, \\ &\boldsymbol{\phi}_{\upsilon}(l_{\tau s,i_s}, k_{\text{vir},i_d}^{l_{\tau s,i_s}}), \cdots, \boldsymbol{\phi}_{\upsilon}(l_{\tau s,L_s-1}, k_{\text{vir},L_{\text{T}}}^{l_{\tau s,L_s-1}})],\end{aligned} \tag{33}$$

where the $(lN_{\text{T}} + k, l_{\tau s,i_s} L_d + k_{\text{vir},i_d}^{l_{\tau s,i_s}})$-th element in $\mathbf{\Phi}_{\upsilon}(\mathbf{l}_{\tau s}, \mathbf{k}_{\text{vir}}^{l_{\tau s}})$ can be calculated as described in (8).[2] The Doppler virtual grid corresponding to delay $l_{\tau s,i_s}$ is denoted by $\mathbf{k}_{\text{vir}}^{l_{\tau s,i_s}}$, whose i_d-th element is written as $k_{\text{vir},i_d}^{l_{\tau s,i_s}}$. Then, the channel estimation model can be expressed as

$$\mathbf{y}_{\text{T}}^{\text{DD}} = \mathbf{\Phi}_{\upsilon}(\mathbf{l}_{\tau s}, \mathbf{k}_{\text{vir}}^{l_{\tau s}})\mathbf{h}_{\upsilon} + \mathbf{z}_{\text{T}}^{\text{DD}}, \tag{34}$$

where $\mathbf{h}_{\upsilon} \in \mathbb{C}^{L_s L_d \times 1}$ represents the Doppler-domain channel. Similar to the approach in the previous section, the Doppler-domain channel is estimated within a Bayesian framework. For a convenient subsequent analysis of virtual-grid updating, we define the vector $\mathbf{K}_{\text{vir}}^{\mathbf{l}_{\tau s}} \in \mathbb{C}^{L_s L_d \times 1}$ that collects all virtual grids involved in the sensing matrix $\mathbf{\Phi}_{\upsilon}(\mathbf{l}_{\tau s}, \mathbf{k}_{\text{vir}}^{l_{\tau s}})$. It is represented as

$$\mathbf{K}_{\text{vir}}^{\mathbf{l}_{\tau s}} = [(\mathbf{k}_{\text{vir}}^{l_{\tau s,0}})^{\text{T}}, (\mathbf{k}_{\text{vir}}^{l_{\tau s,1}})^{\text{T}}, \cdots, (\mathbf{k}_{\text{vir}}^{l_{\tau s,L_s}})^{\text{T}}]^{\text{T}}. \tag{35}$$

For notation simplicity in the subsequent derivations, $\mathbf{\Phi}_{\upsilon}(\mathbf{l}_{\tau s}, \mathbf{k}_{\text{vir}}^{l_{\tau s}})$ is rewritten as $\mathbf{\Phi}_{\upsilon}(\mathbf{K}_{\text{vir}}^{\mathbf{l}_{\tau s}})$. The virtual grids are also updated by maximizing the posterior distribution, as shown below

$$\begin{aligned}\{\hat{\mathbf{K}}_{\text{vir}}^{\mathbf{l}_{\tau s}}\} &= \arg\max p(\mathbf{K}_{\text{vir}}^{\mathbf{l}_{\tau s}} | \mathbf{y}_{\text{T}}^{\text{DD}}) \\ &\propto \arg\max \ \ln p(\mathbf{y}_{\text{T}}^{\text{DD}}, \hat{\boldsymbol{\gamma}}_{\upsilon}, \hat{\alpha}_{\upsilon}, \mathbf{K}_{\text{vir}}^{\mathbf{l}_{\tau s}}) \\ &\propto \arg\max \ f(\mathbf{K}_{\text{vir}}^{\mathbf{l}_{\tau s}}),\end{aligned} \tag{36}$$

where $f(\mathbf{K}_{\text{vir}}^{\mathbf{l}_{\tau s}})$ is given by

$$\begin{aligned}f(\mathbf{K}_{\text{vir}}^{\mathbf{l}_{\tau s}}) = &-\|\mathbf{y}_{\text{T}}^{\text{DD}} - \mathbf{\Phi}_{\upsilon}(\mathbf{K}_{\text{vir}}^{\mathbf{l}_{\tau s}})\boldsymbol{\mu}_{\upsilon}\|_2^2 \\ &- \text{tr}((\mathbf{\Phi}_{\upsilon}(\mathbf{K}_{\text{vir}}^{\mathbf{l}_{\tau s}}))^{\text{H}} \mathbf{\Phi}_{\upsilon}(\mathbf{K}_{\text{vir}}^{\mathbf{l}_{\tau s}}) \mathbf{\Sigma}_{\upsilon}).\end{aligned} \tag{37}$$

Additionally, it should be noted that when updating the parameter $\mathbf{K}_{\text{vir}}^{\mathbf{l}_{\tau s}}$, all other parameters are kept fixed. Since the optimization problem in (36) is non-convex, it is challenging to achieve the optimal solution directly. Therefore, we employ a gradient descent framework with a fixed step size as [28]

$$\hat{\mathbf{K}}_{\text{vir}}^{\mathbf{l}_{\tau s}} = \mathbf{K}_{\text{vir}}^{\mathbf{l}_{\tau s}} + \alpha_{\text{step}} \text{sign}(\nabla f(\mathbf{K}_{\text{vir}}^{\mathbf{l}_{\tau s}})), \tag{38}$$

where α_{step} represents the step size for the update and sign denotes the signum function. Each element in the gradient $\nabla f(\mathbf{K}_{\text{vir}}^{\mathbf{l}_{\tau s}})$ can be represented as

$$\begin{aligned}\frac{\partial f(\mathbf{K}_{\text{vir}}^{\mathbf{l}_{\tau s}})}{\partial K_{\text{vir},i}^{\mathbf{l}_{\tau s}}} =& 2\text{Re}\Big((\mathbf{y}_{\text{T}}^{\text{DD}})^{\text{H}} \frac{\partial \mathbf{\Phi}_{\upsilon}(\mathbf{K}_{\text{vir}}^{\mathbf{l}_{\tau s}})}{\partial K_{\text{vir},i}^{\mathbf{l}_{\tau s}}} \boldsymbol{\mu}_{\upsilon}\Big) \\ &-2\text{Re}\Big(\boldsymbol{\mu}_{\upsilon}^{\text{H}} \mathbf{\Phi}_{\upsilon}^{\text{H}}(\mathbf{K}_{\text{vir}}^{\mathbf{l}_{\tau s}}) \frac{\partial \mathbf{\Phi}_{\upsilon}(\mathbf{K}_{\text{vir}}^{\mathbf{l}_{\tau s}})}{\partial K_{\text{vir},i}^{\mathbf{l}_{\tau s}}} \boldsymbol{\mu}_{\upsilon}\Big) \\ &-2\text{Re}\Big(\frac{\partial \boldsymbol{\phi}_{\upsilon}^{\text{H}}(K_{\text{vir},i}^{\mathbf{l}_{\tau s}})}{\partial K_{\text{vir},i}^{\mathbf{l}_{\tau s}}} \sum_{j=0}^{L_s L_d - 1} \mathbf{\Sigma}_{\upsilon_{j,i}} \boldsymbol{\phi}_{\upsilon}(K_{\text{vir},j}^{\mathbf{l}_{\tau s}})\Big),\end{aligned} \tag{39}$$

where $K_{\text{vir},i}$ ($K_{\text{vir},j}$) denotes the i-th (j-th) element in $\mathbf{K}_{\text{vir}}^{\mathbf{l}_{\tau s}}$ and $\boldsymbol{\phi}_{\upsilon}(K_{\text{vir},i}^{\mathbf{l}_{\tau s}})$ ($\boldsymbol{\phi}_{\upsilon}(K_{\text{vir},j}^{\mathbf{l}_{\tau s}})$) denotes the i-th (j-th) column in $\mathbf{\Phi}_{\upsilon}(\mathbf{K}_{\text{vir}}^{\mathbf{l}_{\tau s}})$.

In summary, the proposed DC-BL algorithm for DD-domain channel estimation with low virtual grid resolution is outlined in **Algorithm** 2. To provide a clear illustration of the sensing matrix refinement process, a flowchart of parameter updating is presented in Fig. 4.

Algorithm 3 DC-BL Algorithm for Fractional Delays and Doppler shifts

```
Input: the truncated received signal $\mathbf{y}_{\text{T}}^{\text{DD}}$, the delay-domain sensing matrix $\mathbf{\Phi}_{\tau}(\mathbf{l}_{\text{vir}}, \mathcal{S}(i_{\tau}))$, the threshold $\epsilon_{\tau}$, $\epsilon_{\text{END}}$, the maximum iteration $k_{\max}$, the number of separations $I_{\text{Sep}}$.
    Delay-domain channel estimation:
    if $r_{\tau}$ is small then
        Follow the steps $1 - 6$ in Algorithm 1 to estimate the delay-domain channel.
    else
        repeat
            Calculate $\boldsymbol{\mu}_{\tau}^{k}$ and $\mathbf{\Sigma}_{\tau}^{k}$ by (15) and (16)
            Update the hyper-parameters $\boldsymbol{\gamma}_{\tau}^{k+1}$, $\alpha_{\tau}^{k+1}$ and $\mathbf{l}_{\text{vir}}^{l_{\tau s},k+1}$ by (18), (19) and (40)
        until $\|\boldsymbol{\mu}_{\tau}^{k+1} - \boldsymbol{\mu}_{\tau}^{k}\|_2^2 \le \epsilon_{\text{END}}$ or $k = k_{\max}$
    end if
    Doppler-domain channel estimation:
    if $r_{\upsilon}$ is small then
        Follow the steps 7-17 in Algorithm 1
    else
        Follow the steps 2-7 in Algorithm 2
    end if
Output: Channel gains, the normalized delay taps, the normalized Doppler shifts
```

C. Channel Estimation based on DC-BL for Fractional Delays and Doppler Shifts

With limited system bandwidth, the effects of fractional delays become non-negligible and must be considered. In this case, the Doppler-domain channel estimation method is consistent with those in **Algorithms** 1 and 2. For delay estimation, we categorize the cases into two scenarios based on the virtual-grid resolution r_{τ} in the delay domain. When the r_{τ} is high, the Bayesian learning based algorithm can be directly

---

[1] Note that for each selected delay tap, three consecutive regions of length Δ_1 were extracted.

[2] For notational consistency, we reuse the symbol $\mathbf{\Phi}_{\upsilon}$ to denote the Doppler-domain sensing matrix, and the construction of its elements is different from that in (28).

TABLE II
COMPARISON OF CHANNEL ESTIMATION ALGORITHMS

Method	Supported waveform	Pilot structure
2D off-grid SBL [24]	Ideal	Kronecker-structured
2D off-grid decomposition and SBL combination [25]	Ideal	Single pilot or single row pilot or single column pilot
DC-BL	Ideal & practical	No restriction

applied for estimation. However, when r_τ is relatively low, the delay-domain virtual grids are treated as unknown parameters and updated iteratively in the Bayesian learning framework. Since the derivation process follows a similar approach as the one in equations (36), (37), and (38) in the previous subsection, we will not elaborate further here, but directly provide the update formula for the delay-domain virtual grids as follows

$$\hat{\mathbf{l}}_{\text{vir}} = \mathbf{l}_{\text{vir}} + \alpha_{\text{step}} \text{sign}(\nabla f(\mathbf{l}_{\text{vir}})). \tag{40}$$

The steps of DC-BL for fractional delay taps is summarized in **Algorithm** 3.

D. Convergence and Computational Complexity Analysis

This subsection presents an analysis of the convergence and computational complexity of the DC-BL algorithms. For delay estimation, Bayesian learning is employed. As Bayesian learning-based method follows the EM framework, convergence has been empirically validated.

In Doppler-domain channel estimation, as outlined in **Algorithm** 1, the region containing the true Doppler shift taps is iteratively refined. At each iteration, the Doppler-domain channel estimation is modeled as an SSR problem and solved by SBL. This implies that the Doppler-domain channel estimation process is also convergent.

In **Algorithm** 2, the delay estimation process remains identical to that in **Algorithm** 1. Although parameterized dictionary learning is employed for Doppler-domain channel estimation, the parameter updates are still carried out within the EM algorithm framework. Besides, by retaining only the updated grids that increase the likelihood function, the fixed step-size grid update method is able to achieve convergence. In summary, the proposed algorithms are guaranteed to converge.

Next, we analyze the computational complexity of the proposed DC-BL algorithm. Since the delay estimation procedures are identical in **Algorithms** 1 and **Algorithm** 2, they share the same computational cost. The overall computational complexity for delay estimation is $\mathcal{O}(L_\tau L_{\text{seg}}(M_{\text{T}}^2 N_{\text{T}}^2 + L_\tau^2 L_{\text{seg}}^2 + M_{\text{T}} N_{\text{T}} L_\tau L_{\text{seg}}))$. For the high-resolution case presented in **Algorithm** 3, the computational complexity of delay estimation is $\mathcal{O}(L_\tau L_{\text{seg}}(M_{\text{T}}^2 N_{\text{T}}^2 + L_\tau^2 L_{\text{seg}}^2 + M_{\text{T}} N_{\text{T}} L_\tau L_{\text{seg}}))$.

For the case with low delay-domain resolution in **Algorithm** 3, reconstructing the sensing matrix and its derivative with respect to delay incurs a complexity of $\mathcal{O}(M_{\text{T}} M L_\tau (M + N_{\text{T}} N^2 L_{\text{seg}}))$. The gradient $\nabla f(\mathbf{l}_{\text{vir}})$ has a complexity of $\mathcal{O}(M_{\text{T}} N_{\text{T}} L_\tau^2 L_{\text{seg}}^2)$. The total computational complexity of delay estimation per iteration is $\mathcal{O}(M_{\text{T}} N_{\text{T}} L_\tau L_{\text{seg}} (M N^2 + L_\tau) + M_{\text{T}} M^2 L_\tau + L_\tau^3 L_{\text{seg}}^3)$.

TABLE III
SIMULATION PARAMETERS

Parameter	Value
Carrier frequency (GHz)	4.9
Subcarrier spacing (kHz)	15
Size of an OTFS symbol, (M, N)	$(256, 16)$
Size of pilot in an OTFS symbol, (M_p, N_p)	$(16, 16)$
Size of guard symbols in an OTFS symbol, (M_g, N)	$(10, 16)$
Maximum normalized delay, $l_{\tau,\max}$	10
Maximum normalized Doppler shift, $k_{\upsilon,\max}$	4
Length of CP, M_{CP}	16
Modulation scheme	4-QAM

Since the SBL algorithm is adopted for Doppler-domain channel estimation with high virtual resolution, the computational complexity per iteration of **Algorithm** 1 and **Algorithm** 3 is $\mathcal{O}(L_s L_{b_i}(M_{\text{T}}^2 N_{\text{T}}^2 + L_s^2 L_{b_i}^2 + M_{\text{T}} N_{\text{T}} L_s L_{b_i}))$.

For the case with low Doppler-domain virtual resolution, the complexity of reconstructing the sensing matrix and its derivative with respect to the Doppler shift is $\mathcal{O}(M_{\text{T}} N_{\text{T}} M N^2 L_s L_d)$ for **Algorithm** 2 and $\mathcal{O}(M_{\text{T}} M L_s (M + L_d N_{\text{T}} N^2)$ for **Algorithm** 3. The computational complexity of the gradient $\nabla f(\mathbf{K}_{\text{vir}}^{\mathbf{l}_{\tau s}})$ is $\mathcal{O}(M_{\text{T}} N_{\text{T}} L_s^2 L_d^2)$. Thus, the per-iteration computational complexity of **Algorithm** 2 and **Algorithm** 3 is given by $\mathcal{O}(L_s L_d (M_{\text{T}} N_{\text{T}} (M N^2 + L_s L_d) + L_s^2 L_d^2))$ and $\mathcal{O}(M_{\text{T}} M^2 L_s + L_s L_d (M_{\text{T}} N_{\text{T}} M N^2 + M_{\text{T}} N_{\text{T}} L_s L_d + L_s^2 L_d^2))$, respectively. The total computational complexity per iteration is summarized in Table V and Table VI.

E. Performance Evaluation

In this subsection, we provide a brief analysis of the performance advantages and underlying sources of improvement of the proposed framework and algorithms. First, leveraging integration, the proposed decoupled channel estimation framework transforms the OTFS channel estimation into separate delay estimation and Doppler-domain channel estimation, providing substantial flexibility in algorithm design to better exploit the distinct characteristics of each domain. Moreover, unlike [24], [25], the inherent generality of the integration operation ensures that the framework is not restricted by waveform constraints and can be applied to arbitrary pulse-shaping filters. Table II summarizes the comparison between the algorithms in [24], [25] and the proposed DC-BL method with respect to waveform compatibility and pilot structure requirements. Second, benefitting from the tap selection mechanism, the proposed DC-BL algorithm effectively reduces the dimensionality of the channel estimation model, achieving a favorable balance between performance and computational complexity. More importantly, the exclusion of certain regions forces the corresponding channel taps to zero, further enhancing the alignment of the DC-BL based estimation result with the intrinsic sparsity in the DD-domain channel and leading to notable improvements in estimation performance.

V. SIMULATION RESULTS

A. Experiment Setup

In this section, the performance of the proposed algorithms is demonstrated through numerical simulation results. Unless stated otherwise, the simulation parameters are as follows. In the simulation, the Extended Vehicular A (EVA) channel model [29] is adopted, and each delay tap corresponds to a single Doppler shift generated by Jakes' formula. At a maximum user equipment (UE) speed of 777 km/h, the maximum multi-path delay and the maximum Doppler shift of the EVA channel model, rounded up, are approximately $k_{\upsilon,\max} = 4$ and $l_{\tau,\max} = 10$, respectively. The data symbols adopt a normalized constellation, while the pilot symbols are complex numbers with randomly distributed phases. Each pilot symbol maintains the same power as the average power of the data symbols. The guard symbols are placed on both sides of the pilot region along the delay axis, with a size of $M_{\rm g} \times N$ on each side. Detailed parameters are listed in Table III.

The effective DD-domain channel $\mathbf{H}_{\rm eff}^{\rm DD}$ is reconstructed for performance evaluation based on the DD-domain input-output relationship defined in (5) (see (46) in Appendix A). The NMSE of CE is then defined as

$$\text{NMSE} = \frac{\|\mathbf{H}_{\rm eff}^{\rm DD} - \hat{\mathbf{H}}_{\rm eff}^{\rm DD}\|_{\rm F}^2}{\|\mathbf{H}_{\rm eff}^{\rm DD}\|_{\rm F}^2}, \tag{41}$$

where $\hat{\mathbf{H}}_{\rm eff}^{\rm DD}$ represents the effective DD-domain channel of the estimated channel.

The hyper-parameters for the proposed algorithms are set to $a = b = c = d = 1 \times 10^{-4}$. The termination criterion is defined as $\epsilon_{\rm END} = 1 \times 10^{-4}$, and $I_{\rm sep}$ is set to 2. For the case of high Doppler-domain resolution, Δ_1 is set to 0.5 and Δ_2 is assigned to $\Delta_2 = r_\upsilon = 0.1$. In the case of low Doppler-domain resolution, Δ_1 is set to 0.8, with Δ_2 given by $\Delta_2 = r_\upsilon = 0.4$.

For comparison, the NMSE performance of the proposed algorithms is compared with several state-of-the-art OTFS channel estimation algorithms, including "Orthogonal matching pursuit (OMP)" [30], "Newtonized orthogonal matching pursuit (NOMP)" [31], "SBL" [21], "2D on-grid SBL" [24] and "2D off-grid SBL" [24]. "Threshold-based channel estimation (Threshold)" [12] employs a sensing matrix without virtual grids as a benchmark algorithm to represent the basic performance. Furthermore, a baseline, called "Oracle", is developed to characterize the performance limit of the proposed algorithms, which is based on SBL with exact delay and Doppler taps [24]. Given that the delay and Doppler shift taps are known, the algorithm only needs to iteratively update the channel gain and the hyper-parameters with (15), (16), (18) and (19).

B. Parameter Analysis

In this subsection, we analyze the impact of parameters ϵ_τ and $L_{\rm seg}$ on the performance of the proposed algorithms. For clarity in the subsequent analysis, we define two metrics:

- Selection rate $N_{\rm sel}/P$: The proportion of the number of true delay taps within the selected range $N_{\rm sel}$ relative to the total number of true delay taps P.
- Over-selection rate $N_{\rm os}/L_{\rm s}$: The proportion of over-selected delay taps $N_{\rm os}$ relative to the total number of selected delay taps $L_{\rm s}$.

TABLE IV
THRESHOLD SETTINGS FOR DIFFERENT SNR LEVELS

SNR (dB)	**Threshold ϵ_τ**	**Virtual resolution**
$[-10, 0]$	0.998	$r_\tau = 0.1/0.4$, $r_\upsilon = 0.1/0.4$
$(0, 15]$	0.999	
> 15	0.9995	
$[-10, 0]$	0.998	$r_\tau = 1$, $r_\upsilon = 0.1/0.4$
$(0, 15]$	0.999	
> 15	> 0.9995	

For generality, the simulation is conducted under the channel with fractional delays and Doppler shifts, where $r_\tau = r_\upsilon = 0.1$.

1) The Impact of Threshold: Firstly, the impact of the threshold ϵ_τ on the performance of the proposed algorithm is analyzed. Fig.5 illustrates the relationship between the selection rate and the threshold ϵ_τ, with SNR set to -10, 0, 10, 20 and 30 dB. It can be observed that as the threshold increases, the selection rate gradually increases and approaches 1, indicating that a higher threshold is more likely to include the true channel taps. Under the same threshold setting, the selection rate decreases with decreasing SNR, except at -10 dB SNR. The intense noise at -10 dB SNR severely distorts the received signal, resulting in poor estimation performance. Additionally, the power distribution of the estimated delay taps becomes more dispersed, leading to the inclusion of a substantial number of redundant taps when the cumulative power ratio reaches the threshold. As a result, the probability of selecting the true taps increases significantly, leading to the markedly higher selection rate observed at -10 dB SNR compared to other SNR levels.

Fig.6 shows the relationship between the over-selection rate and the threshold ϵ_τ. At -10 dB SNR, high noise power introduces spurious impulsive responses at locations unrelated to the true channel, resulting in the erroneous selection of false tap positions and an increased over-selection rate. As the threshold rises, the over-selection rate increases across all SNR levels. At –10 dB SNR, although the over-selection rate is already high when the threshold is set to 0.998, approximately 15% of ineffective delay taps are eliminated, thereby reducing the computational burden of subsequent channel estimation to some extent. Under high SNR conditions, the over-selection rate shows an increasing trend as the threshold rises, yet the extent of the increase remains relatively limited. At an SNR of 30 dB, even when the threshold reaches 0.9995, nearly 65% of the taps are eliminated, as the energy is primarily concentrated around the positions corresponding to the true taps.

Fig. 7 illustrates the impact of the threshold ϵ_τ on the NMSE performance. As shown in the figure, at SNR values of 20 dB and 30 dB, the impact of noise is negligible, resulting in the channel energy remaining largely concentrated on the true channel taps. Consequently, increasing the threshold further suppresses the residual noise, leading to improved NMSE performance. However, at an SNR of 10 dB, the NMSE starts to rise when the threshold exceeds 0.998. Due to the influence of noise, a few of false taps exhibit higher energy than the true ones. As a result, when the threshold is set excessively high, some true taps are mistakenly discarded while certain false

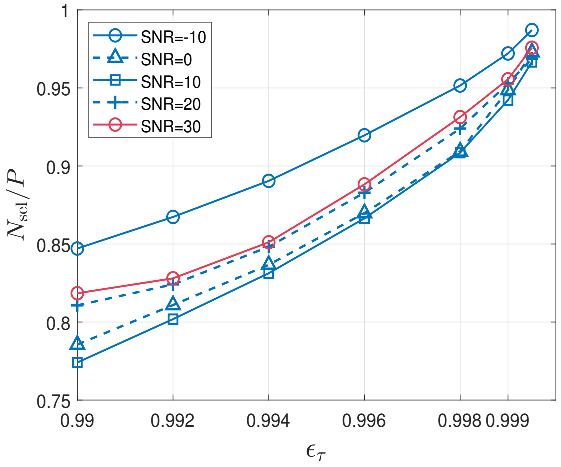

Fig. 5. Selection rate v.s. the threshold ϵ_τ.

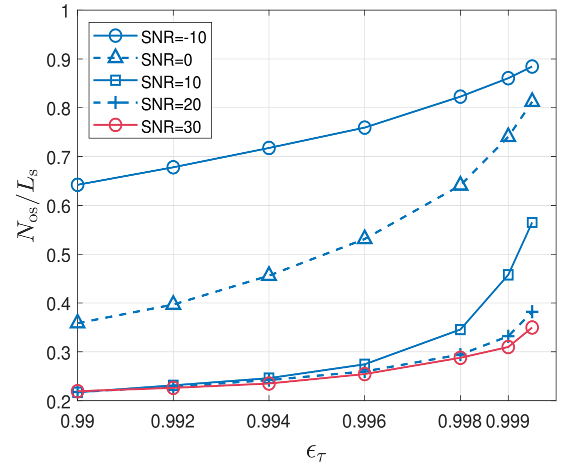

Fig. 6. Over-selection rate v.s. the threshold ϵ_τ.

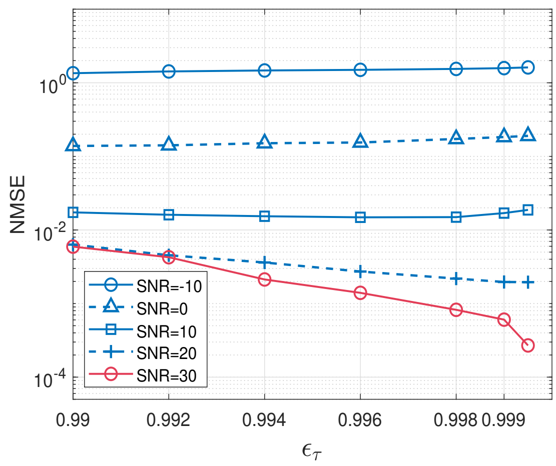

Fig. 7. NMSE v.s. the threshold ϵ_τ with $r_\tau = 0.1$, $r_\upsilon = 0.1$.

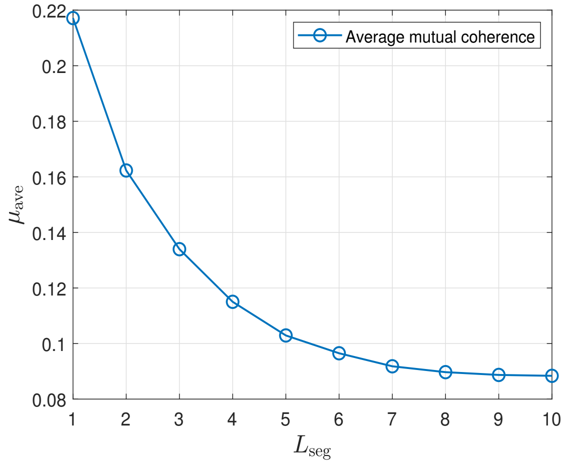

Fig. 8. Average mutual coherence v.s. integration segments L_{seg}.

ones are retained, leading to degraded NMSE performance. At SNR of 0 dB and -10 dB, the NMSE curves remain relatively stable and show little sensitivity to the threshold selection. In summary, the thresholds for different SNR levels are listed in Table IV.

2) The Impact of Number of Doppler-domain Segments: Next, we analyze the impact of the number of Doppler-domain segments on the performance of the proposed algorithm. To evaluate the column correlation of the sensing matrix, the average mutual coherence among its atoms is defined as follows [32]

$$\mu_{\mathrm{ave}} = \frac{1}{2L_{\mathrm{c}}(L_{\mathrm{c}}-1)} \sum_{1\leq i<j\leq L_{\mathrm{c}}}^{L_{\mathrm{c}}} \frac{|\boldsymbol{\phi}_i^{\mathrm{H}}\boldsymbol{\phi}_j|}{\|\boldsymbol{\phi}_i\|_2\|\boldsymbol{\phi}_j\|_2}, \tag{42}$$

where $\boldsymbol{\phi}_i$ and $\boldsymbol{\phi}_j$ represent any two distinct columns of the sensing matrix, and L_{c} denotes the number of columns in the sensing matrix.

Fig.8 depicts the relationship between the average mutual coherence of the sensing matrix and the Doppler-domain integration segments. As L_{seg} increases, the average mutual coherence of the sensing matrix gradually decreases. In general, lower mutual coherence indicates that the sensing matrix can capture richer and more informative features, thereby facilitating the recovery of sparse signals. Consequently, increasing L_{seg} can effectively enhance the performance of channel estimation. When L_{seg} is set to 1, μ_{ave} of the sensing matrix approaches 0.22. Such a high level of mutual coherence is detrimental to the recovery of sparse signals. Compared to the sensing matrix with a single integration, μ_{ave} of the sensing matrix with 4 integration segments is reduced by approximately 47%. When L_{seg} is set to 8, μ_{ave} decreases by about 58.7% compared to the case of a single segment, further enhancing the performance of the sensing matrix.

In the subsequent analysis, L_{seg} is set to 1 for the case of $r_\tau = r_\upsilon = 0.4$ to simplify the delay-grid update and to assess channel estimation performance with Doppler-domain integration over a single segment. L_{seg} is set to 8 for all other cases. The threshold for delay estimation is configured as shown in Table IV.

C. Performance Analysis

1) NMSE Performance under High-Resolution Virtual Grid: Fig.9 presents the NMSE performance of the proposed DC-

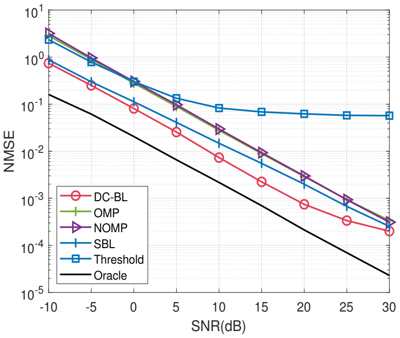

Fig. 9. NMSE v.s. SNR with $r_\tau = 1$, $r_\upsilon = 0.1$.

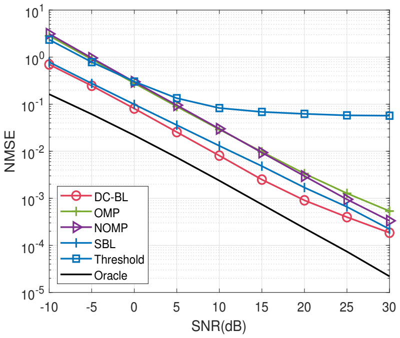

Fig. 10. NMSE v.s. SNR with $r_\tau = 1$, $r_\upsilon = 0.4$.

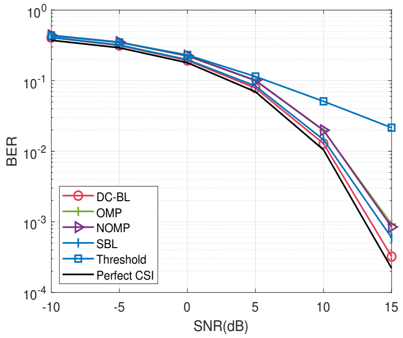

Fig. 11. BER v.s. SNR with $r_\tau = 1$, $r_\upsilon = 0.4$.

TABLE V
COMPUTATIONAL COMPLEXITY (INTEGER DELAY AND FRACTIONAL DOPPLER SHIFTS)

Method	**Computational complexity**
OMP [30]	$\mathcal{O}(M_{\mathrm{T}}N_{\mathrm{T}}L_\tau L_\upsilon + M_{\mathrm{T}}N_{\mathrm{T}}K^2 + K^3)$ (K: the chosen sparsity)
NOMP [31]	$\mathcal{O}(M_{\mathrm{T}}N_{\mathrm{T}}L_\tau L_\upsilon + M_{\mathrm{T}}N_{\mathrm{T}}M^2N^2KR_c + M_{\mathrm{T}}N_{\mathrm{T}}K^2 + K^3)$ (K: the chosen sparsity, R_c: number of cycle refinement)
SBL [21]	$\mathcal{O}(L_\tau L_\upsilon(M_{\mathrm{T}}^2N_{\mathrm{T}}^2 + L_\tau^2L_\upsilon^2 + M_{\mathrm{T}}N_{\mathrm{T}}L_\tau L_\upsilon))$
DC-BL (**Algorithm** 1)	$\mathcal{O}(M_{\mathrm{T}}^2N_{\mathrm{T}}^2(L_\tau L_{\mathrm{seg}} + L_sL_{b_i}) + L_\tau^3L_{\mathrm{seg}}^3 + M_{\mathrm{T}}N_{\mathrm{T}}(L_\tau^2L_{\mathrm{seg}}^2 + L_s^2L_{b_i}^2) + L_s^3L_{b_i}^3)$
DC-BL (**Algorithm** 2)	$\mathcal{O}(M_{\mathrm{T}}^2N_{\mathrm{T}}^2L_\tau L_{\mathrm{seg}} + L_\tau^3L_{\mathrm{seg}}^3 + L_s^3L_d^3 + M_{\mathrm{T}}N_{\mathrm{T}}(L_\tau^2L_{\mathrm{seg}}^2 + MN^2L_sL_d + L_s^2L_d^2))$

BL algorithm (Algorithm 1) compared with state-of-the-art OTFS channel estimation methods across various SNR levels. The virtual grid resolutions are configured as $r_\tau = 1$ and $r_\upsilon = 0.1$. It is evident that the DC-BL algorithm consistently outperforms competing techniques at all SNR levels. Notably, at 10 dB SNR, the NMSE of the proposed DC-BL algorithm is already lower than 1×10^{-2}, whereas the NMSE of other algorithms has not yet reached this level. At 20 dB SNR, DC-BL attains an NMSE of 7.5×10^{-4}, while the second-best performing on-grid SBL algorithm requires approximately 4.36 dB additional SNR to achieve similar accuracy. As the SNR exceeds 20 dB, the performance gain narrows, primarily because high SNR reduces the impact of noise and concentrates energy on true channel tap positions, reducing the influence of discarded regions. By pruning low-contribution channel regions, the DC-BL algorithm achieves significant model dimensionality reduction, thereby lowering computational complexity, as detailed in Table V.

2) Performance with Coarse Doppler Resolution: Fig.10 shows the NMSE performance against SNR with a relatively low virtual-grid resolution, $r_\upsilon = 0.4$. As a result, the DC-BL switches to Algorithm 2. It is observed that the proposed DC-BL algorithm consistently achieves the lowest NMSE across the entire SNR range, indicating its superior performance compared to other schemes. Moreover, by reducing the channel length through the selection process, the proposed algorithm also achieves relative low computational complexity. It is noteworthy that within the proposed DC-BL algorithm, the Doppler-domain channel estimation is carried out alongside a parametric dictionary learning based Bayesian learning algorithm. This highlights the high flexibility offered by the proposed framework, allowing the channel estimation algorithm to be tailored to the specific characteristics of the channel, thereby optimizing estimation performance. Although updating the virtual grid and reconstructing the sensing matrix introduce some computational burden and slow down convergence, the virtual grid update leads to a larger likelihood function and improved estimation performance.

3) BER Performance under Imperfect CSI: Fig.11 illustrates the bit error rate (BER) performance against SNR based on the estimated channel. A similar trend is observed between BER and NMSE, where algorithms achieving lower NMSE tend to provide better BER performance. Within the SNR range of -10 dB to 15 dB, the proposed algorithm achieves a BER performance that closely approaches that of perfect CSI.

4) NMSE Robustness to OTFS Parameters: Fig. 12 demonstrates the NMSE performance versus SNR under an alternative set of OTFS system parameters, specifically $M = 128, N = 32, M_{\mathrm{p}} = 8, M_{\mathrm{g}} = 5$ and $N_{\mathrm{p}} = 32$. The virtual grid resolution is set to $r_\tau = 1$ and $r_\upsilon = 0.1$. As shown in the figure, DC-BL achieves the best performance compared with other baseline algorithms, clearly demonstrating its robustness with respect to OTFS system parameters.

5) NMSE Performance under Aged Channel: Fig. 13 illustrates the NMSE performance of the DC-BL algorithm under different levels of channel aging. To characterize the channel aging effect, following [33]–[35], the aged channel $\mathbf{h}_{\mathrm{Age}}$ is defined as a function of initial channel $\mathbf{h}_0$ and an innovation component, as given below.

$$\mathbf{h}_{\mathrm{Age}} = \rho\mathbf{h}_0 + \sqrt{1-\rho^2}\mathbf{z}_h, \tag{43}$$

where $\mathbf{z}_h \sim \mathcal{CN}(0, \mathbf{R}_{h_0})$ and $\mathbf{R}_{h_0}$ denotes the covariance of $\mathbf{h}_0$. The parameter $\rho \leq 1$ represents correlation coefficient between $\mathbf{h}_0$ and $\mathbf{h}_{\mathrm{Age}}$. For clarity, only the SBL algorithm, which achieved the second best NMSE performance in the earlier simulations, is included as the comparison benchmark. As illustrated in the figure, DC-BL consistently achieves better NMSE performance than SBL under identical correlation coefficients. The NMSE performance decreases as the coefficient ρ decreases, particularly in the high-SNR region, whereas in the low-SNR regime, the NMSE is much less sensitive to

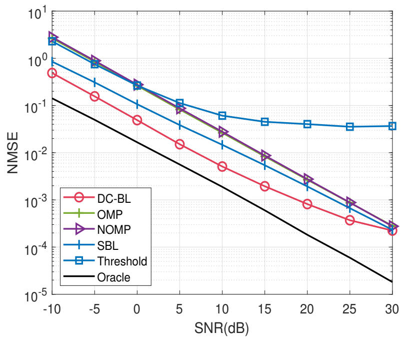

Fig. 12. NMSE v.s. SNR with $r_\tau = 1$, $r_\upsilon = 0.1, M = 128, N = 32$.

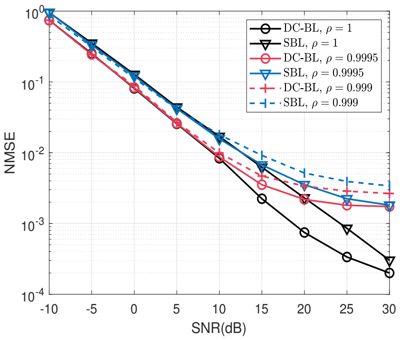

Fig. 13. NMSE under aging channel with $r_\tau = 1, r_\upsilon = 0.1$ and $\rho = 1, 0.9995, 0.999$.

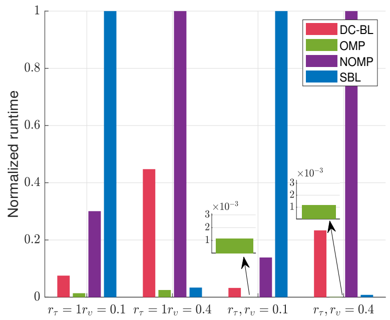

Fig. 14. Normalized runtime.

the coefficient ρ. When the SNR exceeds 20 dB, the NMSE reduction slows down, and the curve gradually flattens.

6) Runtime under Fixed BER: Fig. 14 shows the runtime of DC-BL and other baselines at a fixed BER of 1×10^{-2}. By interpolation, the corresponding SNR values are determined to be 10.46 dB for DC-BL, 10.77 dB for SBL, 11.45 dB for OMP and 11.44 dB for NOMP. The simulations were conducted on a high-performance computing platform equipped with an Intel i7-14700KF CPU, 32 GB of RAM, and a base clock frequency of 3.4 GHz. To eliminate hardware-related effects and highlight the relative computational cost within configuration, the runtime is normalized by the maximum execution time in each group. It can be observed that under the conditions $r_\tau = 1, r_\upsilon = 0.1$ and $r_\tau = 0.1, r_\upsilon = 0.1$, the DC-BL algorithm exhibits significantly lower runtime than both NOMP and SBL, demonstrating its ability to effectively reduce computational complexity in scenarios with large model dimensions and high virtual-grid resolution. When $r_\tau = 1, r_\upsilon = 0.4$ and $r_\tau = 0.4, r_\upsilon = 0.4$, the runtime of the DC-BL algorithm becomes higher than that of SBL. This is mainly attributed to the relatively small model dimension under these settings, combined with the additional computational burden introduced by the grid-refinement process in DC-BL, which collectively give SBL a lower overall computational cost. In addition, although OMP shows a clear advantage in terms of computational efficiency, its estimation performance remains significantly limited.

7) Channel Estimation with Fractional Delay and Doppler: Fig.15 shows the NMSE performance over different SNR levels, with both fractional delay and fractional Doppler shift taken into account. The virtual grid resolutions are set to $r_\tau = 0.1$ and $r_\upsilon = 0.1$, respectively. The inclusion of fractional delay taps significantly increases the 1D DD-domain channel length and the SBL algorithm's complexity. Therefore, it is excluded from the comparison. It can be seen that the proposed DC-BL algorithm achieves the optimal NMSE performance across the entire SNR range. By excluding regions that lack channel taps, the DC-BL algorithm effectively suppresses unnecessary estimation errors, leading to improved performance. Furthermore, the proposed algorithm reduces the computational complexity by effectively lowering the dimensionality of the channel estimation model through the elimination of components that do not contain true channel taps. The computational complexity is shown in Table VI.

TABLE VI
COMPUTATIONAL COMPLEXITY (FRACTIONAL DELAYS AND DOPPLER SHIFTS)

Method	**Computational complexity**
OMP [30]	$\mathcal{O}(M_\mathrm{T} N_\mathrm{T} L_\tau L_\upsilon + M_\mathrm{T} N_\mathrm{T} K^2 + K^3)$ (K: the chosen sparsity)
NOMP [31]	$\mathcal{O}(M_\mathrm{T} N_\mathrm{T} L_\tau L_\upsilon + M_\mathrm{T} N_\mathrm{T} M^2 N^2 K R_c + M_\mathrm{T} N_\mathrm{T} K^2 + K^3)$ (K: the chosen sparsity, R_c: number of cycle refinement)
DC-BL (**Algorithm** 3) $r_\tau = r_\upsilon = 0.1$	$\mathcal{O}(M_\mathrm{T}^2 N_\mathrm{T}^2 (L_\tau L_\mathrm{seg} + L_s L_{b_i}) + L_\tau^3 L_\mathrm{seg}^3 + M_\mathrm{T} N_\mathrm{T} (L_\tau^2 L_\mathrm{seg}^2 + L_s^2 L_{b_i}^2) + L_s^3 L_{b_i}^3)$
DC-BL (**Algorithm** 3) $r_\tau = r_\upsilon = 0.4$	$\mathcal{O}(M_\mathrm{T} N_\mathrm{T} (M N^2 (L_\tau L_\mathrm{seg} + L_s L_d) + L_\tau^2 L_\mathrm{seg} + L_s^2 L_d^2) + L_\tau^3 L_\mathrm{seg}^3 + L_s^3 L_d^3$ $M_\mathrm{T} M^2 (L_\tau + L_s))$

8) Robustness under Coarse Delay and Doppler Resolution: Fig.16 compares the NMSE performance versus SNR with $r_\tau = r_\upsilon = 0.4$. As shown in the figure, the proposed algorithm continues to achieve the best performance across the entire SNR range. The result suggests that the proposed method maintains reliable channel estimation performance even when integration is carried out over only a single segment of the Doppler domain. Moreover, due to the relatively low virtual-grid resolutions in both the delay and Doppler domains, the parametric dictionary learning based estimation method is applied to both domains, which demonstrates the flexibility of the proposed algorithm. While updating the virtual grids in both the delay and Doppler domains increases computational complexity to some extent, it leads to improved NMSE performance. Moreover, the reduced model dimensionality effectively offsets much of the additional complexity.

9) Comparison with 2D On-Grid SBL and 2D Off-Grid SBL under Ideal Waveform Conditions: Fig.17 presents the NMSE performance of the proposed DC-BL algorithm alongside that of the 2D on-gird SBL and 2D off-grid SBL algorithms (collectively referred to as 2D SBL hereafter). An OTFS system employing the ideal waveform with the bi-orthogonal property is considered in this scenario. The virtual grid resolutions are set to $r_\tau = 0.1$ and $r_\upsilon = 0.1$, respectively. It can be seen that both 2D SBL algorithms exhibit nearly identical performance, indicating that the high-resolution virtual grid can capture the

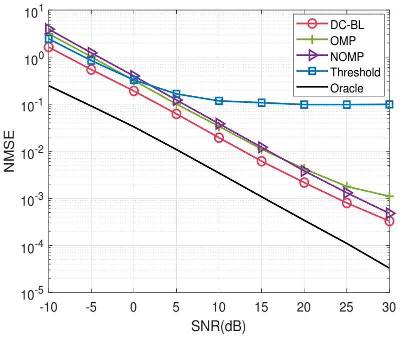

Fig. 15. NMSE v.s. SNR with $r_\tau = 0.1$, $r_\upsilon = 0.1$.

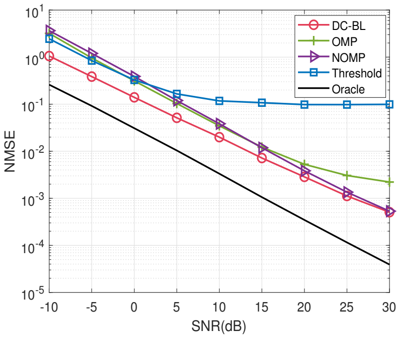

Fig. 16. NMSE v.s. SNR with $r_\tau = 0.4$, $r_\upsilon = 0.4$.

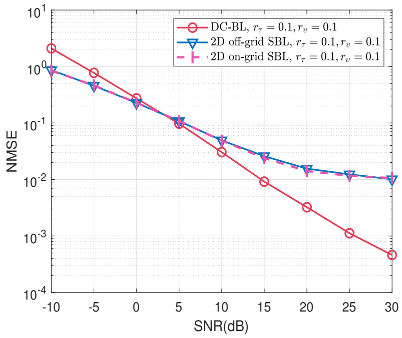

Fig. 17. NMSE v.s. SNR with the ideal waveform.

TABLE VII
COMPUTATIONAL COMPLEXITY (IDEAL WAVEFORM)

Method	**Computational complexity**
2D on-grid SBL [24]	$\mathcal{O}(N_\mathrm{T}L_\upsilon^2 + L_\upsilon^3 + M_\mathrm{T}N_\mathrm{T}L_\tau + L_\tau^2)L_\tau$
2D off-grid SBL [24]	$\mathcal{O}(N_\mathrm{T}L_\upsilon^2 + L_\upsilon^3 + M_\mathrm{T}N_\mathrm{T}L_\tau + L_\tau^2)L_\tau$
DC-BL (**Algorithm** 3) $r_\tau = r_\upsilon = 0.1$	$\mathcal{O}(M_\mathrm{T}^2N_\mathrm{T}^2(L_\tau L_\mathrm{seg} + L_sL_{b_i}) + L_\tau^3L_\mathrm{seg}^3 + M_\mathrm{T}N_\mathrm{T}(L_\tau^2L_\mathrm{seg}^2 + L_s^2L_{b_i}^2) + L_s^3L_{b_i}^3)$

channel structure effectively, and that accounting for off-grid estimation provides negligible improvement. At SNR below 5 dB, both 2D SBL methods achieve better NMSE performance than DC-BL. However, when the SNR exceeds 5 dB, the DC-BL outperforms both 2D SBL schemes. Moreover, the DC-BL achieves an NMSE below 1×10^{-2} at an SNR of 15 dB, whereas the 2D SBL algorithms reach a similar level at 30 dB SNR.

The computational complexity is represented in Table VII. In 2D on-grid SBL and 2D off-grid SBL algorithms, Doppler shifts are estimated based on the delay-domain channel estimation results. Consequently, the channel length is shorter than that in DC-BL, leading to lower computational complexity for the 2D SBL algorithms. However, since the delay-domain channel estimation inevitably introduces estimation errors, the performance of both 2D SBL algorithms is inferior to that of the DC-BL algorithm especially in high SNR conditions. Moreover, neither of the 2D SBL algorithms can be applied to practical systems, which constrained the applicability in practice significantly.

VI. CONCLUSION

In this paper, we proposed a decoupled channel estimation framework for OTFS systems, in which the DD-domain channel is partitioned into delay estimation and the joint estimation of Doppler shift and channel gain. The approach effectively exploits the channel characteristics in delay and Doppler domains, leading to enhanced estimation performance. Based on the framework, we developed a DC-BL channel estimation algorithm. By leveraging virtual grids and integration-based sensing matrices, the proposed algorithm achieves superior performance compared to state-of-the-art schemes. In addition, the proposed algorithm exhibits significant flexibility when applied to virtual grids with relatively low resolution. For such scenarios, an alternative DC-BL channel estimation method is specifically designed to accommodate low-resolution conditions while still delivering satisfactory estimation performance. Furthermore, the proposed algorithms maintain relatively low computational complexity without compromising estimation performance.

APPENDIX A
DERIVATION OF (5)

By substituting (2) into (3), the sampled received signal can be expressed as

$$r(n,l) = \frac{1}{\sqrt{M}} \sum_{i=0}^{P-1} \sum_{m=0}^{M-1} h(l_{\tau_i}, k_{\upsilon_i}) X^{\mathrm{TF}}[n,m] \times e^{\frac{j2\pi m(l-l_{\tau_i})}{M}} e^{\frac{j2\pi n k_{\upsilon_i}}{N}} e^{\frac{j2\pi k_{\upsilon_i}(l-l_{\tau_i}+M_{\mathrm{CP}})}{N(M+M_{\mathrm{CP}})}}. \tag{44}$$

Substituting (1) into (44) and applying the Fourier transform, the DD-domain signal can be expressed as

$$Y^{\mathrm{DD}}[k,l] = \sum_{l'=0}^{M-1} \sum_{k'=-N/2}^{N/2} H_{k,l}^{\mathrm{DD}}[k',l'] X^{\mathrm{DD}}[k',l'] + z^{\mathrm{DD}}[k,l], \tag{45}$$

where the effective DD-domain channel $H_{k,l}^{\mathrm{DD}}[k',l']$ can be represented as

$$\begin{aligned} &H_{k,l}^{\mathrm{DD}}[k',l'] \\ &= \sum_{i=0}^{P-1} \sum_{m=0}^{M-1} \sum_{n=0}^{N-1} h(l_{\tau_i}, k_{\upsilon_i}) e^{\frac{-j2\pi m l'}{M}} e^{\frac{j2\pi n k'}{N}} e^{\frac{j2\pi m(l-l_{\tau_i})}{M}} \\ &\quad \times e^{\frac{-j2\pi n(k-k_{\upsilon_i})}{N}} e^{\frac{j2\pi k_{\upsilon_i}(l-l_{\tau_i}+M_{\mathrm{CP}})}{N(M+M_{\mathrm{CP}})}} \\ &= \sum_{i=0}^{P-1} h(l_{\tau_i}, k_{\upsilon_i}) \Theta_N(k-k'-k_{\upsilon_i}) \Theta_M(-(l-l'-l_{\tau_i})) \\ &\quad \times e^{\frac{j2\pi k_{\upsilon_i}(l-l_{\tau_i}+M_{\mathrm{CP}})}{N(M+M_{\mathrm{CP}})}}, \end{aligned} \tag{46}$$

where $\Theta_N(x) = 1/N \sum_{q=0}^{N-1} e^{-j2\pi xq/N}$ and $\Theta_M(x) = 1/M \sum_{q=0}^{M-1} e^{-j2\pi xq/M}$.

APPENDIX B
DERIVATION OF (20)

The $(lN_{\mathrm{T}}+k, l_\tau)$-th element in $\mathbf{\Phi}_\tau$ can be rewritten as

$$\begin{aligned}\mathbf{\Phi}_\tau(lN_{\mathrm{T}}+k, l_\tau) = &\sum_{l'=0}^{M-1}\sum_{k'=\lceil -N/2\rceil}^{\lceil N/2\rceil} X^{\mathrm{DD}}[k', l'] \\ &\times \Theta_M(-(l-l'-l_\tau))\Gamma_\tau, \end{aligned} \tag{47}$$

where Γ_τ is denoted as

$$\begin{aligned}\Gamma_\tau = &\int_{k_{\upsilon 1}}^{k_{\upsilon 2}} \frac{1}{N}\sum_{n=0}^{N-1} e^{\frac{-j2\pi n(k-k')}{N}} e^{\frac{j2\pi\nu(n+\eta_\tau)}{N}} d\nu \\ =&\frac{1}{N}\sum_{n=0}^{N-1} e^{\frac{-j2\pi n(k-k')}{N}} e^{\frac{j2\pi k_{\upsilon 2}(n+\eta_\tau)}{N}} \frac{N}{j2\pi(n+\eta_\tau)} \\ -&\frac{1}{N}\sum_{n=0}^{N-1} e^{\frac{-j2\pi n(k-k')}{N}} e^{\frac{-j2\pi k_{\upsilon 1}(n+\eta_\tau)}{N}} \frac{N}{j2\pi(n+\eta_\tau)}, \end{aligned} \tag{48}$$

where we denote $(l-l_\tau+M_{\mathrm{CP}})/(M+M_{\mathrm{CP}})$ as η_τ.

REFERENCES

[1] Z. Wei, W. Yuan, S. Li, J. Yuan, G. Bharatula, R. Hadani, and L. Hanzo, “Orthogonal time-frequency space modulation: A promising next-generation waveform,” *IEEE Wireless Commun.*, vol. 28, no. 4, pp. 136–144, 2021.

[2] M. H. C. Garcia, A. Molina-Galan, M. Boban, J. Gozalvez, B. Coll-Perales, T. Şahin, and A. Kousaridas, “A tutorial on 5G NR V2X communications,” *IEEE Commun. Surv. Tutor.*, vol. 23, no. 3, pp. 1972–2026, 2021.

[3] T. Xue, H. Zhang, H. Ding, and D. Yuan, “Joint vehicle pairing, spectrum assignment and power control for sum-rate maximization in NOMA-based V2X underlaid cellular networks,” *IEEE Internet Things J.*, vol. 12, no. 12, pp. 22 337–22 349, 2025.

[4] S. Gyawali, S. Xu, Y. Qian, and R. Q. Hu, “Challenges and solutions for cellular based V2X communications,” *IEEE Commun. Surv. Tutor.*, vol. 23, no. 1, pp. 222–255, 2020.

[5] K. Sehla, T. M. T. Nguyen, G. Pujolle, and P. B. Velloso, “Resource allocation modes in C-V2X: from LTE-V2X to 5G-V2X,” *IEEE Internet Things J.*, vol. 9, no. 11, pp. 8291–8314, 2022.

[6] C.-H. Tseng, P.-H. Chou, and C.-D. Chung, “Sparse-training-sequence-aided OFDM systems for CFO effect mitigation,” in *Proc. IEEE/CIC Int. Conf. Commun. China (ICCC)*, 2014, pp. 303–308.

[7] S. Nagaraj and M. Sarkar, “Inter-carrier interference reduction technique for backscattered OFDM,” *IEEE Trans. Veh. Technol.*, vol. 73, no. 8, pp. 12 237–12 241, 2024.

[8] T. V. S. Sreedhar and N. B. Mehta, “Refined bounds for inter-carrier interference in OFDM due to time-varying channels and phase noise,” *IEEE Wireless Commun. Lett.*, vol. 11, no. 12, pp. 2522–2526, 2022.

[9] R. Hadani, S. Rakib, M. Tsatsanis, A. Monk, A. J. Goldsmith, A. F. Molisch, and R. Calderbank, “Orthogonal time frequency space modulation,” in *Proc. IEEE Wireless Commun. Network. Conf. (WCNC)*, 2017, pp. 1–6.

[10] P. Raviteja, K. T. Phan, Y. Hong, and E. Viterbo, “Interference cancellation and iterative detection for orthogonal time frequency space modulation,” *IEEE Trans. Wireless Commun.*, vol. 17, no. 10, pp. 6501–6515, 2018.

[11] S. Li, J. Yuan, W. Yuan, Z. Wei, B. Bai, and D. W. K. Ng, “Performance analysis of coded OTFS systems over high-mobility channels,” *IEEE Trans. Wireless Commun.*, vol. 20, no. 9, pp. 6033–6048, 2021.

[12] P. Raviteja, K. T. Phan, and Y. Hong, “Embedded pilot-aided channel estimation for OTFS in delay–Doppler channels,” *IEEE Trans. Veh. Technol.*, vol. 68, no. 5, pp. 4906–4917, 2019.

[13] M. Kollengode Ramachandran and A. Chockalingam, “MIMO-OTFS in high-Doppler fading channels: Signal detection and channel estimation,” in *Proc. IEEE Glob. Commun. Conf (GLOBECOM)*, 2018, pp. 206–212.

[14] L. Guo, P. Gu, J. Zou, G. Liu, and F. Shu, “DNN-based fractional Doppler channel estimation for OTFS modulation,” *IEEE Trans. Veh. Technol.*, vol. 72, no. 11, pp. 15 062–15 067, 2023.

[15] W. Yuan, S. Li, Z. Wei, J. Yuan, and D. W. K. Ng, “Data-aided channel estimation for OTFS systems with a superimposed pilot and data transmission scheme,” *IEEE Wireless Commun. Lett.*, vol. 10, no. 9, pp. 1954–1958, 2021.

[16] M. Zhou, F. Chen, M. Xia, X. Zhang, and H. Yu, “Iterative Channel Estimation for Multi-User OTFS Uplink Systems With Superimposed Full Pilots,” *IEEE Trans. Veh. Technol.*, vol. 74, no. 3, pp. 4485–4497, 2024.

[17] D. Donoho, “Compressed sensing,” *IEEE Trans. Inf. Theory*, vol. 52, no. 4, pp. 1289–1306, 2006.

[18] W. Shen, L. Dai, J. An, P. Fan, and R. W. Heath, “Channel estimation for orthogonal time frequency space (OTFS) massive MIMO,” *IEEE Trans. Signal Process.*, vol. 67, no. 16, pp. 4204–4217, 2019.

[19] D. Shi, W. Wang, L. You, X. Song, Y. Hong, X. Gao, and G. Fettweis, “Deterministic pilot design and channel estimation for downlink massive MIMO-OTFS systems in presence of the fractional Doppler,” *IEEE Trans. Wireless Commun.*, vol. 20, no. 11, pp. 7151–7165, 2021.

[20] M. Li, S. Zhang, F. Gao, P. Fan, and O. A. Dobre, “A new path division multiple access for the massive MIMO-OTFS networks,” *IEEE J. Sel. Areas Commun.*, vol. 39, no. 4, pp. 903–918, 2020.

[21] M. Tipping, “Sparse Bayesian learning and the relevance vector machine,” *J. Mach. Learn. Res.*, vol. 1, no. 3, pp. 211–244, SUM 2001.

[22] L. Zhao, W.-J. Gao, and W. Guo, “Sparse Bayesian learning of delay-Doppler channel for OTFS system,” *IEEE Commun. Lett.*, vol. 24, no. 12, pp. 2766–2769, 2020.

[23] S. Srivastava, R. K. Singh, A. K. Jagannatham, and L. Hanzo, “Bayesian learning aided sparse channel estimation for orthogonal time frequency space modulated systems,” *IEEE Trans. Veh. Technol.*, vol. 70, no. 8, pp. 8343–8348, 2021.

[24] Z. Wei, W. Yuan, S. Li, J. Yuan, and D. W. K. Ng, “Off-grid channel estimation with sparse Bayesian learning for OTFS systems,” *IEEE Trans. Wireless Commun.*, vol. 21, no. 9, pp. 7407–7426, 2022.

[25] Q. Wang, Y. Liang, Z. Zhang, and P. Fan, “2D off-grid decomposition and SBL combination for OTFS channel estimation,” *IEEE Trans. Wireless Commun.*, vol. 22, no. 5, pp. 3084–3098, 2022.

[26] Z. Zhang and B. D. Rao, “Sparse Signal Recovery With Temporally Correlated Source Vectors Using Sparse Bayesian Learning,” *IEEE J. Sel. Topics Signal Process.*, vol. 5, no. 5, pp. 912–926, 2011.

[27] M. Butsenko, J. Swärd, and A. Jakobsson, “Estimating sparse signals using integrated wideband dictionaries,” *IEEE Trans. Signal Process.*, vol. 66, no. 16, pp. 4170–4181, 2018.

[28] J. Dai, A. Liu, and V. K. Lau, “FDD massive MIMO channel estimation with arbitrary 2D-array geometry,” *IEEE Trans. Signal Process.*, vol. 66, no. 10, pp. 2584–2599, 2018.

[29] 3GPP, “Evolved Universal Terrestrial Radio Access (E-UTRA); User Equipment (UE) Radio Transmission and Reception,” 3rd Generation Partnership Project (3GPP), Tech. Rep. TS 36.101, March 2024, [Online]. Available: https://www.3gpp.org/.

[30] J. A. Tropp and A. C. Gilbert, “Signal recovery from random measurements via orthogonal matching pursuit,” *IEEE Trans. Inf. Theory*, vol. 53, no. 12, pp. 4655–4666, 2007.

[31] B. Mamandipoor, D. Ramasamy, and U. Madhow, “Newtonized orthogonal matching pursuit: Frequency estimation over the continuum,” *IEEE Trans. Signal Process.*, vol. 64, no. 19, pp. 5066–5081, 2016.

[32] M. Elad, “Optimized projections for compressed sensing,” *IEEE Trans. Signal Process.*, vol. 55, no. 12, pp. 5695–5702, 2007.

[33] R. Chopra, C. R. Murthy, H. A. Suraweera, and E. G. Larsson, “Performance analysis of FDD massive MIMO systems under channel aging,” *IEEE Trans. Wireless Commun.*, vol. 17, no. 2, pp. 1094–1108, 2017.

[34] J. Zheng, J. Zhang, E. Björnson, and B. Ai, “Impact of channel aging on cell-free massive MIMO over spatially correlated channels,” *IEEE Trans. Wireless Commun.*, vol. 20, no. 10, pp. 6451–6466, 2021.

[35] A. Papazafeiropoulos, I. Krikidis, and P. Kourtessis, “Impact of channel aging on reconfigurable intelligent surface aided massive MIMO systems with statistical CSI,” *IEEE Trans. Veh. Technol.*, vol. 72, no. 1, pp. 689–703, 2022.